https://doi.org/10.5194/egusphere-2026-3576
Preprint. Discussion started: 31 July 2026

Drivers of early diagenesis in sediments surrounding offshore wind foundations; a coupled data-modelling approach.

Emil De Borger[1,2], Karline Soetaert[1], Esther Cepeda Gamella[2, 3, 4], Arthur Capet[3, 5], Jan Vanaverbeke [2,3], Ulrike Braeckman[2, 3]

[1] Royal Netherlands Institute of Sea Research (NIOZ), Estuarine and Delta Systems, Korringaweg 7, Yerseke 4401NT, The Netherlands

[2] Ghent University, Marine Biology research group, Building S8 - De Sterre, Krijgslaan 297, 9000 Ghent, Belgium

[3]Royal Belgian Institute of Natural Sciences, Operational Directorate Natural Environment, Marine Ecology and Management, Vautierstraat 29, Brussels 1000, Belgium

[4]Ghent University, Isotope Bioscience laboratory – ISOFYS, Department of green Chemistry and Technology, Coupure links 653, Ghent 9000, Belgium

[5]Université Libre de Bruxelles, Biogeochemistry and modelling of the Earth System, Campus du Solbosch, Avenue F.F. Roosevelt 50, Brussels 1050, Belgium

Correspondence to: Emil De Borger (emil.de.borger@nioz.nl)

Abstract. Permeable sandy sediments are abundant on continental shelves, where they are increasingly recognized as major sites of intense organic matter mineralization. In offshore wind farms (OWFs), turbine-induced changes in hydrodynamics and organic matter inputs may modify these dynamic environments, yet the quantitative impact remains poorly constrained. Here, we present PermeableDia, a two-dimensional reactive transport model that explicitly resolves advective flows and apply it to data collected from sediments along a distance gradient (7-75 m) from the scour protection layer (SPL) of an offshore wind turbine in the Belgian Part of the North Sea across three seasons. The model adequately reproduces observed organic carbon and porewater nutrient profiles and reveals pronounced spatial gradients in carbon mineralization. Total mineralization rates were highest nearest to the turbine (up to ~176 mmol C m^{-2} d^{-1}) and declined with distance. Oxic pathways dominated mineralization (58-92 % of total), reflecting efficient oxygen supply via advective exchange, while anoxic mineralization increased near the turbine (up to 41%) consistent with enhanced organic matter loading. Denitrification contributed only a minor fraction to total mineralization (1 – 4.5 %). By constraining the model with in situ observations, this data-driven approach enables the quantification of mineralization pathways in permeable sediments where direct rate measurements are challenging. The dynamic nature of mineralization processes in advective conditions indicates that observed biogeochemical impacts of offshore wind, such as increased carbon storage in surface sediments, are likely transient.

1 Introduction

Permeable sediments, generally defined as sandy sediment with a permeability exceeding 10^{-12} m^2 cover 50 to 70% of the continental shelf surface (Emery, 1968). Once seen as "(bio-)geochemical deserts" because of their low organic carbon content, permeable sediments have later been recognized as sites of intense organic matter mineralization (B. P. Boudreau et al., 2001). Their high permeability facilitates advective porewater transport, which enhances the exchange of solutes (e.g. oxygen, O_2)

https://doi.org/10.5194/egusphere-2026-3576
Preprint. Discussion started: 31 July 2026

and fine particles (e.g. organic matter) between the sediment and overlying water column (Huettel et al., 2014; Loeff, 1981; Lohse et al., 1996; Webb & Theodor, 1972). This dynamic environment promotes intense organic matter mineralization, as the high availability of oxygen and nitrate fuel degradation of organic matter in the sediment matrix (Ahmerkamp et al., 2020; Cook et al., 2006; Huettel et al., 2014). This makes the permeable sediments of the continental shelf an important link in global nutrient cycles (e.g. C, N, P), as it has been estimated that 17 – 52 % of the global organic matter deposition flux to marine sediments of 1.6 ± 0.6 Pg C y^{-1} is mineralized in these sediments (Dunne et al., 2007; Huettel et al., 2014).

Representing the biogeochemical behaviour of permeable sands in diagenetic models is difficult compared to cohesive (non-permeable) sediments, due to the driving role of advective transport terms which are constrained by the complex interplay of sediment grain characteristics, bedform topography, and local hydrodynamics (Chua et al., 2022; Meysman et al., 2007). Conceptually, however, this is straightforward: local bedform topography (e.g. sand ripples) cause variation in water velocity above the sediment interface which translates into variations in pressure at the spatial scale of bedforms (Bernoulli's principle). This pressure field above the sediment interface (the "pressure head") induces flows of water ("porewater flows") through the sediment matrix from areas of high pressure towards areas of low pressure. These flows are known to extend deep into the sediment, with experimental results establishing advective exchange down to 30 cm depth (Precht & Huettel, 2004). While cohesive sediments are almost always represented in a vertical 1D framework, flows induced by horizontal pressure gradients can only be represented in two dimensions as these go beyond diffusion driven transport. It is thus necessary to employ at least a 2D model to represent diagenesis in permeable sands, which increases the complexity and computational load. Driven by tidal or wave-induced currents, advective flows through the sediment are also highly dynamic, varying strongly in magnitude and direction on timescales of seconds to hours (Huettel et al., 2014). Bedforms themselves are also dynamic features, with sand ripples capable of travelling centimeters per day (R. Soulsby, 1997).

Building on the engineering-based literature on the physical description of flows through and over permeable sediments (e.g. Savant et al., 1987; Shum, 1992; Thibodeaux & Boyle, 1987), various model descriptions have been made to describe (aspects of) diagenesis in permeable sediments, although such applications are much less abundant than works addressing cohesive sediments (Paraska et al., 2014). For example, Shum & Sundby (1996) described how advective flows affect solute distributions and potentially organic matter mineralization. Rutherford et al. (1995) coupled sedimentary flow distributions to relatively simple oxygen kinetics to estimate the contribution of advective flow pumping to the sediment oxygen demand. Several studies focused (mostly) on advective flows generated by (macro)fauna pumping in burrows and the resulting biogeochemical microniches surrounding said burrows (Brand et al., 2013; Meile, 2003; Meysman et al., 2005, 2007). What these models share is their high level of specificity, preventing their wide-scale use to represent larger areas of permeable continental shelf, except for the sand ripple example in Meysman et al. (2007). More extensive modelling of early diagenesis (coupling of advection driven transport to a broader set of chemical reactions) has been done, focused on pollutants (Ren & Packman, 2004, 2005), riverbed biogeochemistry (e.g. Gomez et al., 2012; Zheng et al., 2019), and coupled nitrification-denitrification in marine environments (Cardenas et al., 2008; Cook et al., 2006; Kessler et al., 2012, 2015).

https://doi.org/10.5194/egusphere-2026-3576
Preprint. Discussion started: 31 July 2026

Despite these advances, it appears we still lack a model framework that can be applied to organic matter cycling in permeable sediments over larger spatial (~m) scales. In studies where seafloor biogeochemistry is modelled over larger areas including permeable sediments, the effects of advective flows are often minimized, effectively treating these areas more like cohesive sediments than truly permeable sediments, potentially underestimating the exchange of solutes between water column and seafloor (e.g. Baretta et al., 1995; Capet et al., 2016; De Borger et al., 2021; Wakelin et al., 2012). Because of their one-dimensional representation, cohesive sediment diagenetic modelling is computationally less demanding (see above), and it is much easier to collect the needed data to constrain such models compared to permeable sediments, since measurements in permeable sediments are fraught with difficulties. Whereas the vertical structure of cohesive sediments can be preserved in (widely used) benthic core sampling, sample cores with permeable sediments tend to leak, rapidly disturbing the redox-zonation found in situ. Also, process rate measurements should take place in similar physical (hydrodynamical) conditions as on the seafloor since reaction rates are very dependent on the effects of advective flows. As these advective flows are rarely constant, a range of physical settings should be mimicked in the laboratory to represent variability in time, further complicating work and interpretation of results. In the last two decades, eddy covariance, a non-invasive technique to measure in situ oxygen fluxes integrated over a larger sediment surface has seen increasing use over permeable sediments (as summarized in Berg et al., 2022). While capable of accurately capturing the oxygen dynamics of permeable sediments, other species relevant to early diagenesis (e.g. dissolved inorganic carbon, nitrogen species, phosphate) cannot yet be measured by high frequency sensors needed for eddy covariance to work.

While this “measurement problem” of biogeochemistry in permeable sands remains, we present PermeableDia, a model describing early diagenesis of carbon, nitrogen, and phosphorus in permeable sediments. This modelling package allows for the generation of a porewater flow field induced by a given bedform topography, and its subsequent use as a transport term in addition to diffusive transport in the reactive transport equations of the model components. We offer an open source, and user-friendly modelling framework fit for the purpose of addressing early diagenesis and benthic-pelagic exchanges in the context of permeable sediments at the m^2 scale. Whereas this model is still a 2D representation of the sediment, it is rapidly solved once calibrated.

In this study, we apply PermeableDia to sediments in the immediate vicinity of offshore wind turbines on a permeable sand bank in the Southern Bight of the North Sea (NE Atlantic). Observations of sediment characteristics near these turbines have shown a gradual “fining” of the sediment matrix with inverse distance to the turbines, i.e. a decrease in median grain size paired with an increase in organic matter content (Coates et al., 2014). These patterns have been attributed to i) slightly reduced current velocities in the wake of turbine foundations, allowing finer particles to settle (Legrand et al., 2018), and ii) that an additional input of organic material originates from the fouling fauna growing on the turbine structures (Dannheim et al., 2025; Degraer et al., 2020; Maar et al., 2009). Regardless of the mechanism, such changes in sediment properties are expected to affect sediment biogeochemistry: lower permeability may reduce the role of advective flows, while increasing organic matter availability should elevate mineralization rates and perturb the succession of metabolic pathways (De Borger et al., 2021).

https://doi.org/10.5194/egusphere-2026-3576
Preprint. Discussion started: 31 July 2026

The model case study is constrained with field observations collected during three seasonal campaigns (spring, summer, fall). Sediment characteristics (porewater nutrients, grain size characteristics, organic carbon content and properties) were quantified at 4 fixed distances (7, 15, 25, 75 m) from the edge of the scour protection layer (SPL) of an offshore wind turbine with gravity-based foundation. This scour protection layer consists of a band of rocks of about 25.5 m wide that surrounds the foundation (Peire et al., 2009). Our hypothesis is that turbine presence creates a distance-dependent gradient in sediment properties, which in turn leads to distance-dependent changes in sediment biogeochemical functioning, including total mineralization rates and the relative contribution of different mineralization pathways.

2 Materials and methods

2.1 Data collection

2.1.1 Fieldwork

Sediment core collection

We studied the sediments in immediate vicinity of an offshore wind turbine within the C-Power wind farm concession in the Belgian Part of the North Sea (turbine "D5" at 51° 32,87952' N 2° 55,77318' E, Figure 1 A). This 5MW turbine with gravity based foundation was constructed in 2008 and has been the focus of several environmental studies (e.g. (De Mesel et al., 2015; Kerckhof et al., 2010; Lefaible et al., 2025; Mavraki et al., 2020). We sampled the sediment along a transect extending southwest from the turbine, at distances of 7, 15, 25, and 75 m away from the edge of the SPL, aligned with the direction of the main tidal current (Figure 1 B). Given restrictions on the maneuvering of the research vessel close to the turbines, the samples at 7, 15, and 25 m were collected by scientific divers, whereas at 75 m a NIOZ boxcorer was deployed from a research vessel to sample sediments.

A scientific dive team collected nine perspex cores of 3.6 cm inner diameter (Ø) at each distance: six for the extraction of porewater nutrients, and three to six for the determination of granulometry to investigate grain size trends, and pigments and total organic carbon (TOC) to quantify organic carbon sources. The cores were pressed into the seafloor by hand, aiming for 15 cm of sediment in the cores, and sealed with a rubber stopper. The cores were then carefully lifted out of the seafloor and sealed below as well. The cores were placed into a PVC rack, to keep them upright during transport to the support vessel.

From the research vessel, the NIOZ boxcore (Ø 30 cm) was lowered to the seafloor at 75 m away from the edge of the SPL and retrieved after closing. From the undisturbed boxcore, nine subcores (Ø 3.6 cm) were collected: 5 for the extraction of porewater nutrients, and 4 for the same environmental parameters as described above.

This sampling scheme was replicated seasonally when possible. In summer the NIOZ boxcore was not available to take samples at 75 m distance; in winter, no samples were collected due to unfavorable weather conditions, see Table S.1 for an overview of sampling dates and conditions.

https://doi.org/10.5194/egusphere-2026-3576
Preprint. Discussion started: 31 July 2026

Sediment trap procedure

To estimate organic matter deposition rates within the OWF, a sediment trap mounted on a tripod was deployed seasonally at a site 200 m southwest of turbine D5 (Cepeda-Gamela et al., *in prep.*). This trap consisted of an open-ended PVC tube (1000 mm length, 125 mm diameter), without side-holes. At the bottom end of the tube, a funnel shaped appendage with threads allowed for the attachment of a 250 mL recipient filled with tap water. Traps were mounted on a tripod 1 m above the sediment water interface.

The tripod mounted trap was deployed from 3 to 12 days. Upon recovery, recipients were carefully unscrewed, collecting any overflow in a bucket to avoid sample loss and kept at -20 °C until further analysis. Once in the lab, the collected material was weighed and subdivided for different analysis using a splitter to promote equal distribution of the samples. Then, half of the samples were stored with 4% formaldehyde and the other half stored by freezing at -20 °C.

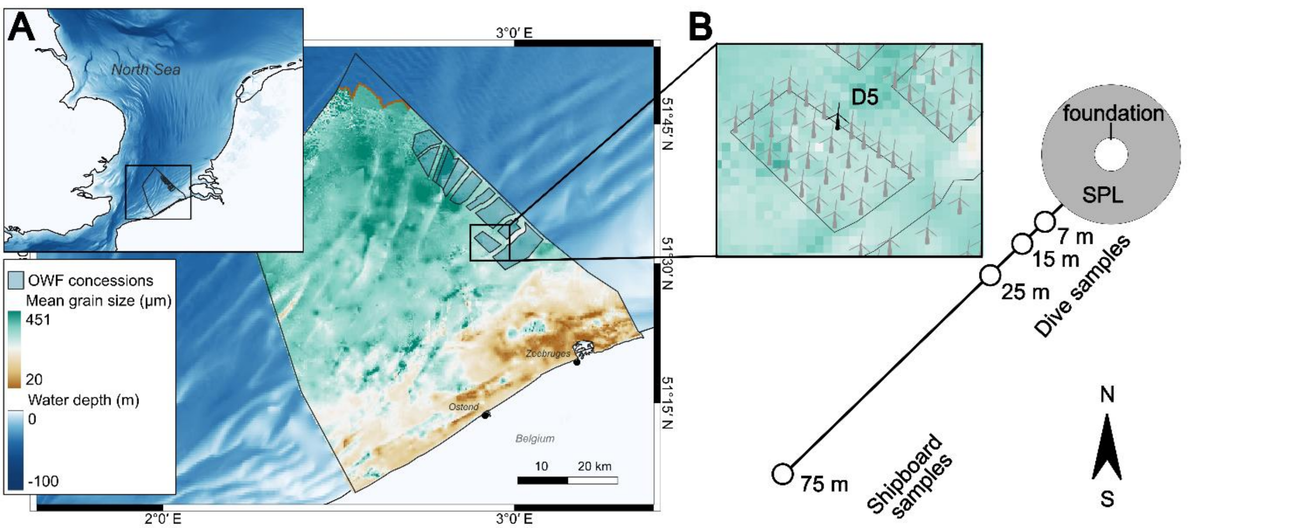

Figure 1: Location of the study with (A) the median grain size in the Belgian EEZ (brown-green gradient), locations of the offshore wind concessions (blue polygons), and its setting within the North Sea (inset top right). (B) location of turbine "D5" in the C-Power concession, and sampling design surrounding the turbine. Grain size data and turbine location layers retrieved from RBINS (*RBINS Metadata Catalog*, 2025), bathymetry from GEBCO (*Gridded Bathymetry Data | GEBCO*, 2024).

2.1.2 Sample analysis

Sedimentary characteristics

Cores for the sedimentary characteristics were sliced into 1 cm sections, throughout the length of the retrieved cores. Cores were placed upright onto an extruder, where the overlying water was carefully siphoned off without disturbing the sediment surface. Then the core was pushed upwards, cm by cm, and each section was stored separately in an aluminium cap vial and stored at -80 °C until further processing.

These sediment samples were freeze-dried for further analysis. The water content (weight fraction) was determined as the volume of water removed by freeze-drying wet sediment samples. Porosity was then determined from water content and solid

https://doi.org/10.5194/egusphere-2026-3576
Preprint. Discussion started: 31 July 2026

phase density measurements, accounting for the salt content in the porewater. The grain size distribution (median grain size in µm and distribution) was determined using laser diffraction on a Malvern Mastersizer 2000G, hydro version 5.40. From median grain size (D_{50}), sediment permeability was derived following Wilson et al. (2018) (Eq. 1). TOC (% of sediment dry weight) content of the sediment was determined using an Interscience Flash 2000 organic elemental analyzer (uncertainty: 0.01%, standard used: sulphanilamide). Photosynthetic pigment contents (chlorophyll *a*, pheophorbide, pheophytin) were measured on the freeze-dried samples, through HPLC analysis after Wright & Mantoura (1997).

$$Permeability = 10^{-9.213} D_{50}^{4.615} \quad \text{(Eq. 1)}$$

Porewater nutrients

Porewater was extracted from the cores with rhizon samplers (0.15 µm, Rhizosphere Research Products) through pre-drilled holes. A sample of the overlying water in the cores was collected by inserting a rhizon sampler in the surface water and collecting ~5 mL into a vial. Rhizons, pre-soaked in low nutrient filtered seawater flushed with N_2 gas to reduce exposure of porewater to oxygen were inserted into the sediment and a maximum of 3 mL of porewater was extracted from each interval by connecting a 3 mL syringe and creating a vacuum (Dickens et al., 2007; Seeberg-Elverfeldt et al., 2005; Shotbolt, 2010). Porewater nutrients were stored frozen (-20 °C) until further processing. Once thawed, nutrient samples were analysed by a SEAL QuAAtro segmented flow analyser (Jodo et al., 1992).

Sediment trap analysis

Half of the frozen subsamples were used for carbon analysis. Those were treated to remove as much chloride from the sample as possible to prevent damage to the analyzing machines. Therefrom, samples were centrifuged with a 0.01 M calcium sulphate 3 times (3500 rpm for 5 min), discarding each time the supernatant. The sediment fraction was then freeze dried for 24 hours and stored at – 80 °C. From the freeze-dried samples 5 mg were taken for total carbon analysis and packed into tin cups. For organic carbon analysis, 40 mg were taken into silver cups and fumigated with 37% HCl for 24 hours, then freeze-dried and packed into tin cups for analysis with an EA–IRMS (Elemental Analyzer–Isotope Ratio Mass Spectrometry).

2.2 Model setup

2.2.1 Model description

We used the permeableDia model (Soetaert & De Borger, in prep.), a model of early diagenesis which includes advective flows as a transport mechanism. In this model, a variable pressure head across the seabed surface is imposed, mimicking how bedforms (e.g. sand dunes, sand ripples, burrow extensions, ..) create variations in current speeds and induce pressure gradients across the sediment water interface. The pressure head then drives solute flows through the sediment matrix, which also vary depending on the sediment porosity and permeability. This approach requires a 2D model grid, describing a sediment cross-section of *y* m deep, along a length of *x* m of seabed surface, where *x* and *y* can be arbitrarily specified.

In practice, the flow in permeable sediments is generated in two steps.

First, a boundary value problem is solved for the hydraulic head h (in m, Eq. 2), or pressure P(in kg m^{-1} s^{-2}):

https://doi.org/10.5194/egusphere-2026-3576
Preprint. Discussion started: 31 July 2026

$$s\frac{\partial h}{\partial t} = \frac{1}{A}\nabla A\left[\frac{-\rho g \kappa}{\mu}\nabla h\right] + \sum G_h \quad \text{(Eq. 2)}$$

With $A_{\square}$ the surface area (m^2), κ the permeability (m^2), s the storativity (m^{-1}), μ the dynamic viscosity of the porewater ($kg\ m^{-1}\ s^{-1}$), ρ the seawater density ($kg\ m^{-3}$), and g the gravitational constant ($m\ s^{-2}$). G_h is the source or sink of the hydraulic head (s^{-1}), calculated as the flow rate per unit of volume. The more general form of Eq. 1 that considers density variations is given by (Eq. 3):

$$\frac{s}{g}\frac{\partial P}{\partial t} = \frac{1}{A}\nabla A_x\rho\left[\frac{-\kappa}{\mu}(\nabla P + \delta\rho g)\right] + \sum G_P \quad \text{(Eq. 3),}$$

Where δ is 1 for the vertical axis and 0 for the horizontal axis (i.e. the effect of horizontal density gradients on flows is ignored). From the above the pressure head h (m), the pore water velocity, υ ($m\ s^{-1}$), is estimated as:

$$\phi\upsilon = \frac{-\rho g \kappa}{\mu}(\nabla h) \quad \text{(Eq. 4)}$$

or

$$\phi\upsilon = \frac{-\kappa}{\mu}(\nabla P + \delta\rho g) \quad \text{(Eq. 5),}$$

where ϕ is the porosity.

The boundary condition in the horizontal axis x imposes a zero-gradient in horizontal velocity at the domain edges (x = 0, Lx). This allows movement in or out of the domain (Eq. 6):

$$\frac{\partial^2 h}{\partial x^2}\Big|_{x=(0,Lx)} = 0 \quad \text{(Eq. 6)}$$

For the vertical (y-direction), the pressure head is imposed (f) near the surface (y = 0), while zero-gradient flows are assumed at the lower boundary (Ly) (Eq. 7).

$$\frac{\partial^2 h}{\partial y^2}\Big|_{y=(Ly)} = 0; h(x)|_{y=0} = f(x) \quad \text{(Eq. 7)}$$

The pressure head near the surface is derived from local seabed topography and granulometric information (see 2.2.2.1).

The advective flows (Eq. 4) are used in combination with diffusive terms to transport solutes in the sediment matrix. The biogeochemical formulations are based on the OMEXDIA model of early diagenesis (Soetaert et al., 1996) extended with simplified phosphorus dynamics (Ait Ballagh et al., 2020). This diagenetic model is a 3G-description of organic matter mineralization (OM) in marine sediments, i.e. where organic matter consists of three “fractions” that differ in their degradability: highly degradable (fresh), intermediate degradable (older), and refractory (non-degradable). The two reactive fractions of organic matter are degraded at fixed specific rates, whereas the mineralization pathways vary depending on the availability of oxidants (Table 1): oxic mineralization when oxygen is available, denitrification when the oxygen concentration is low and nitrate is available, anoxic mineralization in the absence of oxygen and nitrate (processes such as sulfate reduction, manganese reduction, iron reduction,… are lumped together). In total, the model state variables comprise four solid species (fast and slow degrading organic matter FDET and SDET respectively, iron bound phosphorus FeP, and calcium bound phosphorus CaP), and 6 solute species (oxygen O_2, nitrate NO_3^-, ammonia NH_3, “Oxygen Demand Units” - ODU’s, phosphate

https://doi.org/10.5194/egusphere-2026-3576
Preprint. Discussion started: 31 July 2026

PO_4^{3-}, and dissolved inorganic carbon DIC). Here ODU are the lump sum of reduced products of anoxic mineralization (sulphide, iron and manganese ions), expressed in the amount of oxygen required to reoxidize them.

Dynamics of the solid (Eq. 8) and solute (Eq. 9) species C_i are governed by the reactive transport equation (Boudreau, 1997):

$$(1-\phi)\frac{\partial C_i}{\partial t} = (1-\phi)\nabla(Db\nabla C_i - wC_i) + (1-\phi)R_i \quad \text{(Eq. 8) and}$$

$$\phi\frac{\partial C_i}{\partial t} = \phi\nabla(D_i\nabla C_i - vC_i) + \phi R_i \quad \text{(Eq. 9),}$$

with ϕ the porosity of the sediment matrix, v the pressure driven advective flows described above (m s^{-1}), w the sediment accretion rate, Db the bioturbation coefficient which varies with depth y (Eq. 10), and D_i the molecular diffusion coefficient (D_i^{mol}) corrected for tortuosity (Eq. 11):

$$Db_y = Db_0 e^{\frac{-(y-L_{mix})}{Db_{coeff}}} \quad \text{(Eq. 10)}$$

$$D_i = [1-2ln\phi]^{-1}D_i^{mol} \quad \text{(Eq. 11),}$$

and lastly R_i, the biogeochemical transformations affecting the species i, which are outlined in supplement S1. (Eq. S. 1 – Eq. S. 12 as per Soetaert et al., 1996).

The model was solved to steady state (deriving equilibrium concentrations of state variables for a given set of boundary conditions and parameters), using the "steady" function on the rootSolve package (Soetaert & Herman, 2009).

Table 1: Main diagenetic reactions of the permeableDia model.

Process	Reaction
Oxic mineralization	$(CH_2O)x\ (NH_3)y\ (H_3PO_4) + xO_2 \rightarrow xCO_2 + yNH_3 + H_3PO_4 + xH_2O$
Denitrification	$(CH_2O)x\ (NH_3)y\ (H_3PO_4) + 0.8\ x\ HNO_3 \rightarrow xCO_2 + yNH_3 + 0.4\ x\ N_2 + H_3PO_4 + 1.4\ x\ H_2O$
Anoxic mineralization	$(CH_2O)x\ (NH_3)y\ (H_3PO_4)$ + an oxidant $\rightarrow xCO_2 + yNH_3 + H_3PO_4 + xODU + xH_2O$
Nitrification	$NH_3 + 2O_2 \rightarrow HNO_3- + H_2O$
ODU oxidation	$ODU + O_2 \rightarrow$ an oxidant

2.2.2 Parameterization

Model dimensions and Flow field

In the permeableDia workflow, a field of advective flows is first generated based on the local topography (function *permeable.flow*, github repository in prep.). This function also sets the dimensions of the model's grid (Table 3).

We estimated the characteristics of bedforms in the area for each season - distance combination using the empirical relationships between sediment median grain size (d_{50}) and maximal ripple length (λ_{max}) and height (η_{max}) provided by Soulsby et al., (2012) for current generated ripples:

$$\eta_{max} = d_{50}202D_*^{-0.554} \text{ for } 1.2 < D_* < 16 \quad \text{(Eq. 12)}$$

$$\lambda_{max} = d_{50}(500 + 1881D_*^{-1.5}) \text{ for } 1.2 < D_* < 16 \quad \text{(Eq. 13),}$$

https://doi.org/10.5194/egusphere-2026-3576
Preprint. Discussion started: 31 July 2026

with dimensionless grain size D_* calculated as:

$$D_* = [g(sr-1)/v^2]^{1/3} d_{50} \qquad \text{(Eq. 14)},$$

with v the kinematic viscosity of water, sr the density ratio of sediment (ρ) over (sea)water (ρ_s), and g the gravitational constant. In this formula, λ_{max}, η_{max} and d_{50} are expressed in m.

In highly energetic conditions, so-called washout conditions, water movements erode and destroy the crests of established sand ripples, resulting in a flat or featureless seafloor. So for a given set of current conditions and sediment properties we first need to evaluate whether bedform topography has ripple features that cause advective flows. Evaluating the washout condition threshold θ_{wo} using the Shields parameter θ is done following Soulsby et al. (2012) to verify the presence of ripples:

$$\theta = \frac{\tau}{(\rho_s-\rho) g d_{50}} \qquad \text{(Eq. 15)}$$

$$\theta_{wo} = 1.66 D_*^{-1.3} \qquad \text{(Eq. 16)}$$

With variable values: d_{50} = 0.000292 – 0.000435 (m), v = 1.10 – 1.36 10^{-6} ($m^2 s^{-1}$ - temperature-dependent), g = 9.81 ($m s^{-2}$), ρ = 1025 ($kg m^{-3}$), ρ_s= 2650 ($kg m^{-3}$), and τ = 0.6 (Pa; Mean bottom shear stress during one spring-neap tidal cycle for the sampling location as calculated in Van den Eynde et al. (2020).

Applying these formulae to the environmental conditions in the different sampling campaigns resulted in minor variations in maximal ripple height between 1.93 and 2.77 cm, and horizontal wave lengths of 17.2 and 24.6 cm (see Table 2).

Table 2: Parameters used for the calculation of maximal ripple height (η_{max}) and lengths (λ_{max}) for different distance – season combinations, starting from median sediment grain size (µm). salinity (PSU), and temperature (ºC). From these, the Shields parameter (θ), dimensionless grain size (D*), and washout condition (θ_{wo}) were calculated.

season	Distance [m]	Temperature [ºC]	median grain size [µm]	Salinity [PSU]		θ	D^*	θ_{wo}	η_{max} [cm]	λ_{max} [cm]
Spring	7	9	364	33		0.102	7.5	0.119	2.34	20.8
	15	9	339	33		0.109	7.06	0.127	2.48	22.1
	25	9	292	33		0.127	6.15	0.148	2.77	24.6
	100	9	364	33		0.102	7.5	0.119	2.34	20.8
Summer	7	18.5	364	33		0.102	7.85	0.113	2.28	20.3
	15	18.5	384	33		0.097	8.09	0.109	2.17	19.4
	25	18.5	372	33		0.1	7.94	0.111	2.23	19.9
Autumn	7	20	354	33		0.105	7.88	0.112	2.29	20.3
	15	20	392	33		0.095	8.23	0.106	2.12	18.9
	25	20	435	33		0.086	8.94	0.096	1.93	17.2
	100	20	355	33		0.105	7.9	0.112	2.28	20.2

The biogeochemical processes in the sediment porewater below one ripple were modelled down to 1 m deep to satisfy the assumption of negligible gradient that underlies the boundary conditions. This resulted in a model domain of dimensions equal

https://doi.org/10.5194/egusphere-2026-3576
Preprint. Discussion started: 31 July 2026

to the wavelength (x-direction) by 1 m (y-direction). The wavelength was divided into 10 cells in the x-direction. The 1 m depth was divided into 50 cells in the y-direction; the grid size is 0.001 m at the surface, increasing downwards.

With the ripple geometry fixed, the pressure head h at the sediment-water interface was implemented as a sinusoidal wave along the sediment-water interface (Eq. 17):

$$h(x)|_{y=0} = \frac{\eta_{max}}{2}\left[1 + \sin\left(\frac{2\pi x}{\lambda_{max}} - \frac{\pi}{2}\right)\right] \qquad \text{(Eq. 17)}$$

Note that the ripple geometry is used to generate the pressure head, but is not applied to the model geometry itself, which remains flat on the sediment-water interface.

A representative example of the flow field is shown below (Figure 2).

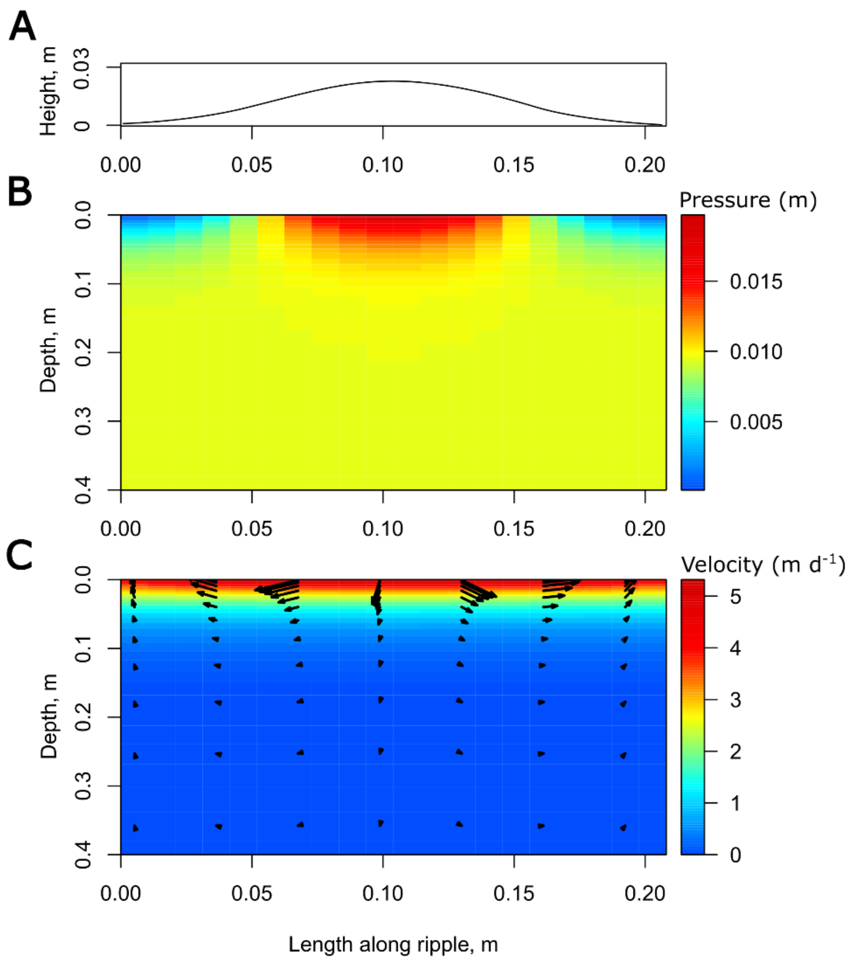

Figure 2: Visualization of a 2 cm high symmetric sand ripple (A), the resulting pressure head (in m B), and advective flow velocity and direction (black arrows, in m d^{-1}, C) in the sediment below that ripple. Only the top 0.4 m of the model domain is shown as advective flows are negligible in deeper layers for our settings (and general cases, see Huettel et al., 2014).

https://doi.org/10.5194/egusphere-2026-3576
Preprint. Discussion started: 31 July 2026

Table 3: Parameterization of the advective flow model (only non-standard values are shown, while default values are described in the "permeableDia" package (Github repository in prep.).

Parameter	Unit	Value / Range	Source
Height domain	m	0.0193 – 0.0277	S1. Supplementary materials and methods
Length domain	m	1	S1. Supplementary materials and methods
Number of cells x-dimension	-	10	
Number of cells y-dimension	-	50	
Max. pressure head	m	See height domain	See Eq. 17 and above.
Porosity	-	0.3	Representative measured value from field
Permeability	m^2	$1.31\ 10^{-11}$- $2.09\ 10^{-12}$	Representative computed value from field
Temperature	ºC	9.9 - 20	Seawater temperature at time of data collection
Salinity	PSU	33.3	Average value field measurements
Specific storativity	m^{-1}	$5.50\ 10^{-5}$	Average value sandy sediments (Chowdhury et al., 2022)

Diagenetic model

While a fitting procedure took place to find optimal parameter values for each season – distance combination (see 2.2.3), initial values and ranges for parameters of the diagenetic model were adapted to shallow permeable sediment where possible (e.g. *rFast*, *rSlow*, *w*, *Db*, *rNit*) (Table S. 3). Mineralization rates of the highly degradable and degradable fractions (*rFast*, *rSlow*) were set to the higher reported values (Arndt et al., 2013), as expected in oxygenated permeable sediments. To determine the initial guess for the carbon input flux (*Cflux*), literature data was compiled to find the range of potential values for the productive coastal setting of the Belgian Part of the North Sea (Table 4). *pFast*, the fraction of highly degradable OM in the incoming carbon flux was kept constant to 0.74 (as in Soetaert et al., 1996), as we did not have data to constrain this parameter simultaneously to *Cflux*, and the mineralization rates. Environmental variables such as bottom water concentrations of solutes were set according to field-data (see Table S. 2 for available field information). Other parameter values were left to the default as described in Soetaert et al. (1996) (Table S. 3).

Table 4: Estimates of organic carbon deposition rates found in literature.

Reported value	Reported unit	mmol C m^{-2} d^{-1}	Location and period - type of estimation	Source
51	gC m^{-2} yr^{-1}	11.6	Overall BPNS estimate – model simulation	Lancelot et al. (2005)

72.4 ± 5.1	gC m^{-2} yr^{-1}	16.5 ± 1.2	Sandy sediment BPNS average annual value – model simulation	Provoost et al. (2013)
4.1 – 13.3	gC m^{-2} d^{-1}	341.7 – 1108.3	Inside OWF measurement	Sediment trap
155 - 320	gC m^{-2} yr^{-1}	35.4 - 73.1	BPNS – model simulation	Joiris et al. (1982)
> 200	mgC m^{-2} d^{-1}	> 16.7	In summer when mussels are producing at their maximum in BPNS OWF – model simulation	Ivanov et al. (2021)
22	mmol C m^{-2} d^{-1}	22	Inside BPNS OWF simulations – model simulation	De Borger et al. (2021)
104 ± 8	Mg km^{-2} yr^{-1}	23.8 ± 1.8	Non-trawled average sandy North Sea sediment – model simulation	Zhang et al. (2024)

2.2.3 Model fitting

Optimizing model parametrizations for reactive transport models such as PermeableDia presents several challenges. First a clear correspondence must be established between simulated and observed biogeochemical species. In this work, model outputs are two-dimensional, whereas field observations consist of one-dimensional vertical sediment profiles. To enable comparison, model results were horizontally averaged into a single vertical profile. This assumes that measured profiles represent a spatial average along ripple structures, which is reasonable given the use of replicate cores and the associated variability (standard deviations) observed in field measurements.

Secondly, several model parameters can have similar effects on output variables, leading to issues of parameter identifiability and collinearity. To counter these issues, several constraints between parameters were imposed based on prior knowledge, in addition to ranges derived from literature discussed above. A 10:1 relation between *rFast* and *rSlow* was imposed, and bioturbation depth *L* was derived from the average reactivity of the organic matter and the bioturbation coefficient *Db*, as specified in Middelburg (2019) (see S1. supplementary materials and methods). The true fitting procedure was performed in successive steps in which subsets of parameters were constrained using selected observations and fitting approaches.

In a first step, initial estimates for fast and slow degradation rates (*rFast*, *rSlow*), bioturbation rate (*Db*), and bioturbation depth (*L*) were determined by manually comparing modelled TOC and NH_3 profiles with measured profiles, and selecting a set of values that could reproduce the major features of all profiles for a range of possible carbon deposition fluxes (*Cflux*), namely: low TOC values, relatively straight TOC profiles, and a low but non-zero NH_3 buildup.

In the second step, the carbon deposition flux (*Cflux*) was constrained for each station using TOC and NH_3 profiles. This was performed using a brute-force screening approach implemented with functions from the R package FME (Soetaert & Petzoldt, 2023). Candidate *Cflux* values between 10 and 250 mmol C m^{-2} d^{-1} were evaluated in increments of 10 mmol C m^{-2} d^{-1}. For each candidate value, model output was compared with observations, and the model cost was calculated as the sum of squared

https://doi.org/10.5194/egusphere-2026-3576
Preprint. Discussion started: 31 July 2026

residuals between measured and modelled profiles. The *Cflux* value minimizing this cost function was retained. This step therefore reduced the plausible range of *Cflux* values prior to the final optimization step.

Since the bottom water temperature varied per season, temperature dependencies were incorporated by applying a Q_{10} factor of 2 to *rFast* and *Db* relative to a reference temperature of 15 °C:

$$rFast(T) = rFast(T_{ref}) \cdot 2^{\frac{T-15}{10}} \quad \text{(eq. 18)}$$

$$Db(T) = Db(T_{ref}) \cdot 2^{\frac{T-15}{10}} \quad \text{(eq. 19)}$$

In the last fitting step, values for a fixed parameter set (*Cflux*, *Db*, *L*, nitrification rate *rNit*, and saturation constants *ksNO3denit* and *ksO2nitri*) were optimized using the "BOBYQA" (Bounded Optimization by Quadratic Approximation) algorithm in the "nloptr" package (Johnson, 2008), where the bounds were set to within 10 – 50 % of the values depending on the parameter (supplement - scripts). The parameters included in this step were selected after evaluating potential parameter collinearity and the sensitivity of model output to individual parameters (Soetaert & Petzoldt, 2023). Model calibration in this final step used measured profiles of TOC, NH_3, and NO_3^-.

Standard deviations around the solutions and parameter estimates were generated through sensitivity analysis. First, the solution space was explored in a Markov Chain Monte Carlo analysis (MCMC, 2000 repetitions), to check for model convergence and to generate a mean and standard deviation around parameter values. This distribution of parameter values was subsequently used to generate uncertainties around model process outputs (using function sensRange, Soetaert & Petzoldt (2023)).

Sensitivity of the model output to changes in the flow regime was also assessed using the sensRange function by altering the parameters storativity, permeability, porosity, ripple length, and ripple height within realistic ranges and identifying the direction of change for integrated mineralization processes (total mineralization, oxic and anoxic mineralization, denitrification, and the relative contributions of the oxic, anoxic mineralization and denitrification to total mineralization).

2.3 Statistical analyses

To assess differences between the measured concentrations of TOC in the sediment, median sediment grain sizes, and pigment content between different seasons, distances, and season - distance interactions, Type II ANOVA's were performed (for unbalanced designs, as summer - 75 m values were not available. Two models were tested per variable, one for surface values (0 – 2 cm), and one for the subsurface layer (> 2 – 12 cm), given that the dynamics deeper in the cores differed from surface observations. Because of the sparse nature of the distances (effectively 3 – 4 discrete stations depending on the season), distance was treated as a categorical factor instead of a continuous predictor. Values per replicate were averaged over the depth range. Assumptions for the ANOVA (homoscedasticity and normality of residuals) were tested using Levene's test for homogeneity of variance and Shapiro-Wilk normality test. If either of these assumptions was not fulfilled (most of the cases), an alternative non-parametric permutation test was performed to provide p-values (9999 permutations, Type II sums of squares, function "aovperm" from the R package "permuco" - Frossard & Renaud (2021)).

https://doi.org/10.5194/egusphere-2026-3576
Preprint. Discussion started: 31 July 2026

No meaningful statistics could be conducted on the model outputs themselves due to the limited number of independent observations remaining (n = 11 unique season – distance combinations). Therefore, we performed a graphical exploration of the relations between a selection of model outputs (total mineralization, rates of oxic, anoxic mineralization and denitrification (mmol C m^{-2} d^{-1}), percentage of these processes of total mineralization (%), and the nitrification rate (mmol N m^{-2} d^{-1}) and hypothesized predictors that were not already explicitly included as model parameters (distance from SPL (m), TOC surface sediment, MGS, pigment concentrations). Loess smoothers were used to visualize potential relationships. Approximate 95 % confidence intervals were calculated from the standard errors of the Loess predictions and shown as bands in the visualization. Different span parameters were explored to assess the robustness of observed trends. As patterns were sensitive to the degree of smoothing, a higher span (1.2) was selected to emphasize general trends and reduce overfitting.
Model simulations and statistical analyses were performed in the RStudio (Posit team, 2022) environment for R (R Core Team, 2021).

3 Results

3.1 Sediment properties

Throughout the measurement period, surface sediment median grain size was significantly affected by the season-distance interaction (interaction $p = 0.009$) and varied between 292 ± 7 µm (spring – 25 m) and 435 ± 56 µm (autumn – 25 m) (Table 5), (Table S. 4). The same goes for the deeper layers (2 – 12 cm, Table S. 5 for averaged values, Figure S. 1 for full profiles), where values at the 25 m distance went from finest to coarsest average values from spring to autumn (interaction $p < 0.001$, Table S. 4).
Surface total organic carbon content (TOC, 0 – 2 cm, Table 5), was highest in spring and summer (0.05 ± 0.01 - 0.08 ± 0.02 %), and significantly lower in autumn (0.03 ± 0.01 - 0.05 ± 0.01 %; season $p = 0.009$, Table S. 4). No significant distance-related patterns were detected for surface TOC values. In deeper layers (2 – 12 cm, Table S. 5), average TOC values showed significant differences between specific season – distance combinations (interaction $p = 0.013$, Table S. 4).
Like TOC, surface chlorophyll *a* (chl *a*) contents were significantly higher in spring (range of 0.2 ± 0.06 µg chl *a* g^{-1} dry sediment to 1.26 ± 0.75 µg g^{-1}; Table 5) compared to other seasons (season $p < 0.001$, Table S. 4). In the subsurface layers (2 – 12 cm, Table S. 5), average values differed more strongly between specific seasons – distance combinations, with this interaction clouding individual responses to either season or distance (interaction $p < 0.001$, Table S. 4).
For surface pheophorbide concentrations, there was significant variability between different season – distance combinations (interaction $p = 0.031$; Table S. 4) that obscured a potential significant difference between seasons as seen in chl *a* content. Highest contents were seen in subsurface samples in spring but otherwise displayed no consistent season or distance related trends (Table S. 4, Table S. 5).

https://doi.org/10.5194/egusphere-2026-3576
Preprint. Discussion started: 31 July 2026

Surface pheophytin values were significantly higher in spring (range 0.01 – 0.14 ± 0.2 µg g^{-1}), compared to autumn (range 0.01 – 0.02 ± 0.01 µg g^{-1}; Table 5). Pheophytin concentrations reached maximum concentrations in deeper sediment layers in spring, as seen in the pheophorbide values (Table S. 5).

Table 5: Measured surface (average top 2 cm ± SD) values for median grain size (MGS, µm), permeability (m^2), total organic carbon (TOC, %), chlorophyll a (Chl a, µg g^{-1}), pheophorbide (µg g^{-1}), and pheophytin (µg g^{-1}).

Season	Distance (m)	MGS (μm)	Permeability	TOC (%)	Chl a ($\mu g\ g^{-1}$)	Pheophorbide ($\mu g\ g^{-1}$)	Pheophytin ($\mu g\ g^{-1}$)
spring	7	364 ± 70	5.77 10^{-12}	0.07 ± 0.04	0.64 ± 0.35	0.05 ± 0.04	0.12 ± 0.14
spring	15	339 ± 32	4.16 10^{-12}	0.05 ± 0.01	0.99 ± 1.24	0.04 ± 0.04	0.14 ± 0.2
spring	25	292 ± 7	2.09 10^{-12}	0.08 ± 0.02	1.26 ± 0.75	0.08 ± 0.05	0.11 ± 0.08
spring	75	364 ± 13	5.77 10^{-12}	0.05 ± 0.01	0.2 ± 0.06	0.01 ± 0	0.01 ± 0
summer	7	364 ± 30	5.77 10^{-12}	0.05 ± 0.01	0.3 ± 0.11	0.03 ± 0.02	0.06 ± 0.02
summer	15	384 ± 23	7.39 10^{-12}	0.05 ± 0.01	0.16 ± 0.05	0.04 ± 0.02	0.04 ± 0.02
summer	25	372 ± 35	6.38 10^{-12}	0.05 ± 0.01	0.22 ± 0.17	0.05 ± 0.05	0.07 ± 0.07
autumn	7	354 ± 15	5.08 10^{-12}	0.04 ± 0.01	0.2 ± 0.08	0.02 ± 0.02	0.01 ± 0
autumn	15	392 ± 35	8.13 10^{-12}	0.05 ± 0.01	0.34 ± 0.09	0.02 ± 0.01	0.02 ± 0.01
autumn	25	435 ± 56	1.31 10^{-11}	0.04 ± 0.01	0.22 ± 0.15	0.01 ± 0.01	0.01 ± 0.01
autumn	75	355 ± 16	5.14 10^{-12}	0.03 ± 0.01	0.17 ± 0.1	0.01 ± 0	0.01 ± 0

3.2 Nutrient profiles

Porewater nutrient concentrations displayed patterns linked to seasonality and distances away from the SPL (Figure 3). In spring, concentrations of ammonia, nitrite and phosphate were highest nearest to the SPL and decreased further away. Nitrate displayed the opposite pattern, as nitrate concentrations increased with distance away from the SPL.

In summer, concentrations of ammonia and phosphate were also highest at 7 m, though the contrast with 15 and 25 m was less pronounced than in spring. Nitrate and nitrite did not display trends with distance in summer.

https://doi.org/10.5194/egusphere-2026-3576
Preprint. Discussion started: 31 July 2026

In autumn, nitrate and phosphate concentrations respectively increased and decreased with increasing distance from the SPL, similar to the spring observations. Ammonia and nitrite concentrations did not display a pattern, though ammonia concentrations were consistently elevated at all distances when compared to the other seasons.

https://doi.org/10.5194/egusphere-2026-3576
Preprint. Discussion started: 31 July 2026
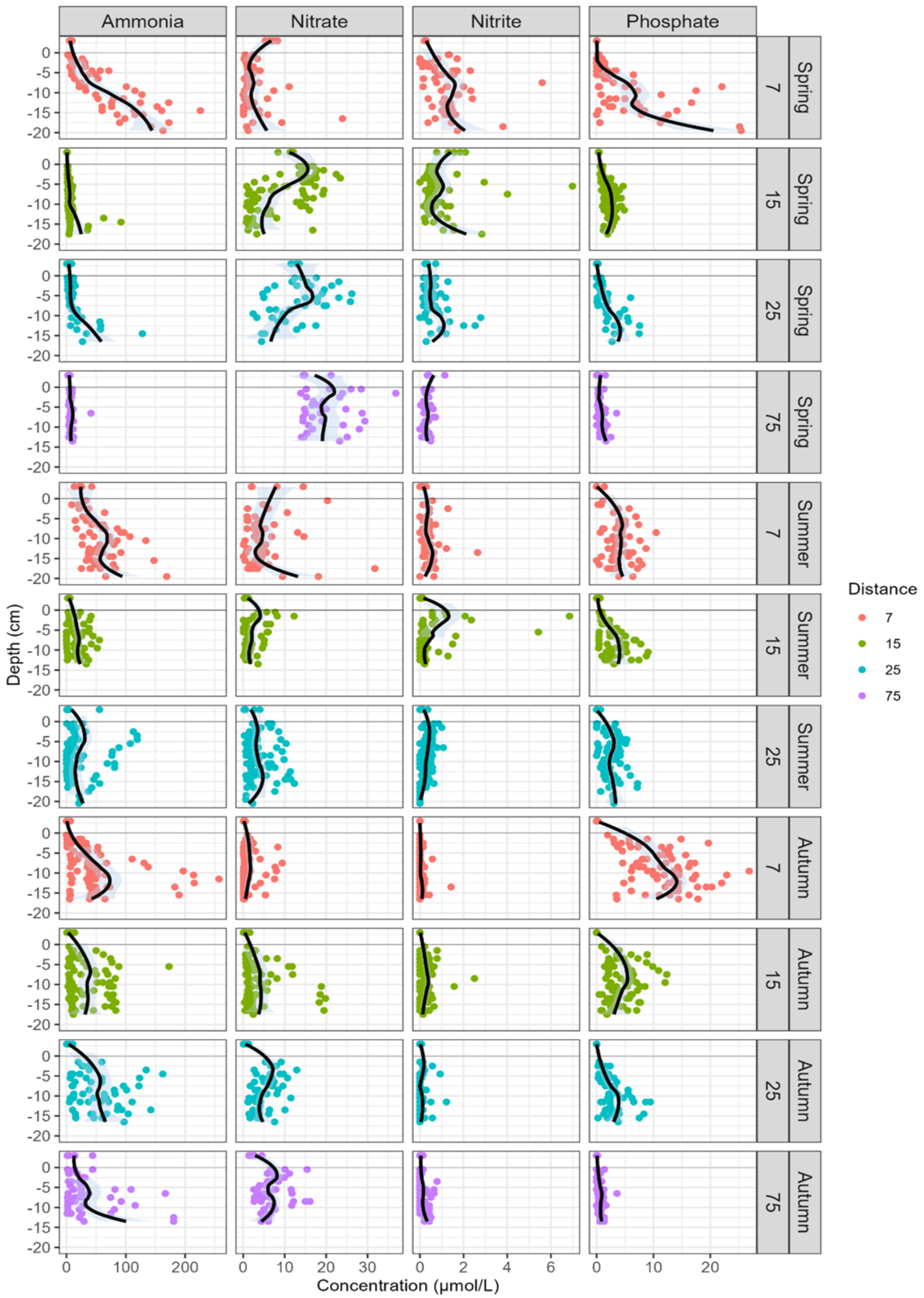
https://doi.org/10.5194/egusphere-2026-3576
Preprint. Discussion started: 31 July 2026

Figure 3: Smoothed (black lines) average porewater nutrient profiles for ammonia (NH_3), nitrate (NO_3^-), nitrite (NO_2^-), and phosphate (PO_4^{3-}) (columns) for the different season – distance combination (rows). Individual values shown by dots.

3.3 Sensitivity analysis

The model was not sensitive to changes in storativity *S* (Figure S. 2, A), and outputs varied only little with changes in porosity, although towards higher porosity the percentage of oxic mineralization decreased slightly, and anoxic mineralization and denitrification increased (Figure S. 2, B). Permeability (κ) strongly affected the magnitude of different mineralization processes: at low permeabilities (1 10^{-13} m^2 – cohesive sediment) almost all (99 %) of mineralization occurred through anoxic mineralization (Figure S. 2, C). This percentage decreased with increasing permeability, while oxic mineralization and denitrification increased in importance. Denitrification reached a peak value at intermediate permeabilities after which it decreased again. The proportion of oxic mineralization continued to increase until all OM mineralization occurred through the aerobic metabolism, at a permeability of 2.5 – 3 10^{-11} m^2 and higher. Ripple length and ripple height (Figure S. 2, D-E) had opposite effects: increasing the ripple length increased the proportion of anoxic mineralization over other processes, while increasing the ripple height strongly increased the proportion of both oxic mineralization and denitrification.

3.4 Best fit – MCMC – parameter estimates

Through the fitting and Markov Chain Monte Carlo (MCMC) procedures, we generated probability distributions around best-fit parameter estimates of all season – distance combinations (Table 6, with full parametrization of each site in Table S. 3). We were able to satisfactorily simulate porewater profiles, especially for NH_3, though the model was incapable of reproducing the straight TOC profiles, or those where TOC values increased with depth (see Figure S. 3 – Figure S. 13).
The incoming carbon flux (*Cflux*) ranged from 53.6 ± 3.1 to 178 ± 3.9 mmol C m^{-2} d^{-1}, with highest values in spring at 7 m, and lowest in spring at 15 m from the SPL. In all seasons, *Cflux* values appeared highest closest to the turbine (7m) and were lower further away. In fall, values for *Cflux* further away (15 and 75 m) were similar to the 7 m values, with a lower value only at the 25 m station(Table 6). Bioturbation rates followed the enforced Q_{10} relation, with higher bioturbation rates in summer – autumn when temperatures were higher (range of $8.65 \cdot 10^{-5} \pm 4.85 \cdot 10^{-6}$ - $9.62 \cdot 10^{-5} \pm 5.32 \cdot 10^{-6}$ m^2 d^{-1}), compared to spring ($5.53 \cdot 10^{-5} \pm 3.22 \cdot 10^{-6}$ - $6.18 \cdot 10^{-5} \pm 2.81 \cdot 10^{-6}$ m^2 d^{-1}). Bioturbation depths varied between 0.14 and 0.16 m in all season – distance combinations. There was relatively little difference between the fitted values for the nitrification rate (*rNit*, 5.8 ± 1.5 - 12.8 ± 1.8 d^{-1}), the half saturation value of nitrate in denitrification (*ksNO3denit*, 11.4 ± 3.3 - 15.9 ± 4.5), and half saturation of oxygen in nitrification (*ksO2nitri*, 13.6 ± 4.4 - 18.3 ± 3.6), and neither did values for these parameters display clear relations to either season or distance. The probability distributions provided by the MCMC procedure for these parameters were then used to generate 2000 simulations to provide uncertainty estimates around main model diagnostics, as reported in Table 6.

Table 6: Best fit parameter estimates and confidence intervals derived from the MCMC procedure, for fitted parameters. Values reported as average value with standard deviation [± SD].

		Cflux	*Bioturbation*	*Bioturbation depth*	*rNit*	*ksNO3denit*	*ksO2nitri*
Season	Distance (m)	mmol C m^{-2} d^{-1}	m^2 d^{-1}	m	d^{-1}	mmolNO_3 m^{-3}	mmolO_2 m^{-3}
Spring	7	178 ± 3.9	$6.18 \cdot 10^{-5} \pm 2.81 \cdot 10^{-6}$	0.156 ± 0.005	9.7 ± 2.5	15.2 ± 4.2	15.4 ± 0.4
	15	53.6 ± 3.1	$5.62 \cdot 10^{-5} \pm 2.85 \cdot 10^{-6}$	0.141 ± 0.007	10.3 ± 1.9	13.9 ± 4.3	15.1 ± 4.4
	25	57 ± 4.1	$5.53 \cdot 10^{-5} \pm 3.22 \cdot 10^{-6}$	0.148 ± 0.007	10.9 ± 2.9	15.9 ± 4.5	14.8 ± 4.2
	75	61.1 ± 5.8	$5.57 \cdot 10^{-5} \pm 2.95 \cdot 10^{-6}$	0.142 ± 0.009	12.8 ± 1.8	14 ± 3.9	13.6 ± 4.4
Summer	7	148.8 ± 4	$8.96 \cdot 10^{-5} \pm 4.87 \cdot 10^{-6}$	0.139 ± 0.005	8.5 ± 2.6	14.3 ± 4.2	15.7 ± 4.6
	15	76.6 ± 4.4	$9.13 \cdot 10^{-5} \pm 3.97 \cdot 10^{-6}$	0.156 ± 0.006	5.8 ± 1.5	11.4 ± 3.3	18.3 ± 3.6
	25	78.9 ± 6	$8.65 \cdot 10^{-5} \pm 4.85 \cdot 10^{-6}$	0.167 ± 0.01	7.8 ± 1.4	14.4 ± 3.9	14.2 ± 4.1
Fall	7	138.7 ± 8.3	$9.43 \cdot 10^{-5} \pm 5.25 \cdot 10^{-6}$	0.14 ± 0.008	9.2 ± 2.7	14.7 ± 4.2	15.7 ± 4
	15	136.7 ± 8.9	$9.33 \cdot 10^{-5} \pm 5.04 \cdot 10^{-6}$	0.135 ± 0.005	10.1 ± 2.3	15.6 ± 4.1	14.5 ± 4.6
	25	73.6 ± 5.4	$9.56 \cdot 10^{-5} \pm 5.03 \cdot 10^{-6}$	0.153 ± 0.008	8.9 ± 2.77	15.8 ± 4.6	15.4 ± 4.5
	75	118.6 ± 6.5	$9.62 \cdot 10^{-5} \pm 5.32 \cdot 10^{-6}$	0.164 ± 0.009	9.4 ± 2.6	14.4 ± 4.3	15.4 ± 4.6

3.5 Mineralization rates and fluxes

Modelled mineralization processes displayed trends between seasons and distances away from the turbine (Figure 4, Table 7). In line with the fitted *CFlux*, the total mineralization values were highest closest to the turbine. This was clearest in spring and summer where values peaked at 176.1 ± 7.7 and 146.4 ± 8.6 mmol C m^{-2} d^{-1} at 7 m and decreased strongly further away to reach values of 61.4 ± 6.9 and 80.1 ± 8.5 mmol C m^{-2} d^{-1} in spring (75 m) and summer (25 m) respectively. In fall, total mineralization rates were more similar between sites (137.5 ± 11.5 – 116.3 ± 10.2 mmol C m^{-2} d^{-1}), though at 25 m there were distinctively lower values (72.3 ± 7.6 mmol C m^{-2} d^{-1}). For the most part, Oxic mineralization was the major mineralization process (ranging from 34.6 to 111.6 mmol C m^{-2} d^{-1}, or 58.6 - 91.8 % of total mineralization), followed by anoxic mineralization (ranging between 5.3 to 72.2 mmol C m^{-2} d^{-1}, or 7.3 – 40.9 % of total mineralization), whereas denitrification took up only a

https://doi.org/10.5194/egusphere-2026-3576
Preprint. Discussion started: 31 July 2026

small part of total mineralization (0.7 – 5.3 mmol C m^{-2} d^{-1}, or 1 – 4.5 % of total mineralization) (Figure 4). Nitrification ranged between 1.3 – 4.2 mmol N m^{-2} d^{-1}.

Table 7: Mineralization rates (mmol m^{-2} d^{-1}), percentages of different mineralization processes of total mineralization (%), and exchange rates (mmol m^{-2} d^{-1}) of the different season x distance from turbine combinations. Values reported as average value with standard deviation [± SD].

Season	Distance	Mineralization rates (mmol C m^{-2} d^{-1})				Percentage of total mineralization			mmol N m^{-2} d^{-1}
		Total	Oxic	Denitrification	Anoxic	Oxic	Denitrification	Anoxic	Nitrification
Spring	7	176.1 ± 7.7	99.7 ± 3	4.2 ± 0.9	72.2 ± 5.4	56.7 ± 1.4	2.4 ± 0.5	40.9 ± 1.4	2.2 ± 0.8
	15	51.9 ± 5.8	44.6 ± 4.1	1.8 ± 0.4	5.5 ± 1.5	86.2 ± 2.2	3.5 ± 0.7	10.3 ± 1.9	1.6 ± 0.5
	25	59.4 ± 6.8	34.6 ± 2	2.7 ± 0.4	22.2 ± 4.9	58.6 ± 3.6	4.5 ± 0.8	36.9 ± 3.9	1.3 ± 0.4
	75	61.4 ± 6.9	53.8 ± 5.2	2.3 ± 0.4	5.4 ± 1.4	87.7 ± 1.6	3.7 ± 0.4	8.7 ± 1.4	2.6 ± 0.4
Summer	7	146.4 ± 8.6	101.6 ± 4.3	5.3 ± 1.4	39.5 ± 5	69.5 ± 2	3.6 ± 1	26.9 ± 1.9	4.2 ± 1.5
	15	79.4 ± 7.5	69.9 ± 6.1	1 ± 0.2	8.5 ± 1.5	88.1 ± 0.9	1.2 ± 0.3	10.6 ± 0.9	2.1 ± 0.5
	25	80.1 ± 8.5	69.1 ± 6.6	1.6 ± 0.5	9.4 ± 1.9	86.3 ± 1.3	2.1 ± 0.6	11.7 ± 1.2	3.3 ± 1
Fall	7	137.5 ± 11.5	95.5 ± 4.7	1.4 ± 0.5	40.5 ± 7.1	69.7 ± 2.7	1 ± 0.4	29.2 ± 2.9	1.5 ± 0.6
	15	135.7 ± 11.9	111.6 ± 8.4	1.6 ± 0.6	22.5 ± 3.8	82.4 ± 1.4	1.2 ± 0.4	16.5 ± 1.5	2.5 ± 0.9
	25	72.3 ± 7.6	66.3 ± 6.7	0.7 ± 0.2	5.3 ± 0.9	91.8 ± 0.6	1 ± 0.3	7.3 ± 0.6	2.2 ± 0.7
	75	116.3 ± 10.2	86.5 ± 5.5	2.9 ± 0.9	27 ± 4.9	74.5 ± 2.3	2.5 ± 0.8	23 ± 2.3	3.1 ± 1.1

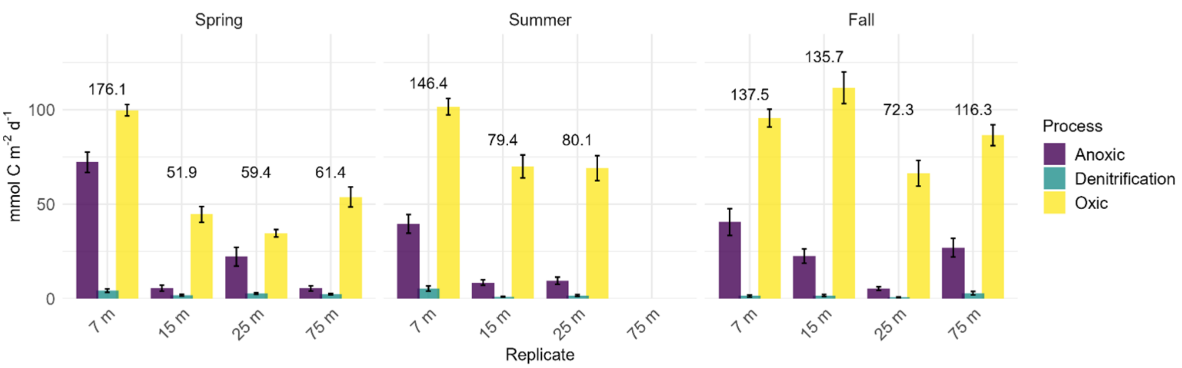

https://doi.org/10.5194/egusphere-2026-3576
Preprint. Discussion started: 31 July 2026

Figure 4: Carbon mineralization process rates (in mmol C m^{-2} d^{-1}, y-axis), grouped per season (panels) – distance (x-axis) from scour protection layer combination. Flags show standard deviation based on 2000 input parameter variations. Values above each bar group are the summed total mineralization (in mmol C m^{-2} d^{-1}).

Table 8: Exchange fluxes between sediment and overlying water (mean ± SD, mmol m^{-2} d^{-1}), where negative values represent fluxes out of the sediment.

Season	Distance (m)	O_2	NH_3	NO_3^-	PO_4^{3-}	DIC
Spring	7	107.4 ± 2.2	-23.6 ± 1.6	1.2 ± 0.2	-1.5 ± 0.1	-176.1 ± 7.7
	15	50.8 ± 4.5	-6 ± 1	-0.2 ± 0.3	-0.4 ± 0.1	-51.8 ± 5.9
	25	38.9 ± 1.6	-7.4 ± 1.2	0.8 ± 0.2	-0.5 ± 0.1	-59.1 ± 6.7
	75	61.6 ± 5.7	-6.3 ± 1.1	-0.8 ± 0.4	-0.5 ± 0.1	-61 ± 6.9
Summer	7	115.1 ± 3.2	-17.2 ± 2.2	0 ± 0.5	-1.2 ± 0.1	-146.6 ± 8.6
	15	78.9 ± 6.4	-9.6 ± 1.2	-1.3 ± 0.3	-0.7 ± 0.1	-79.4 ± 7.5
	25	80.3 ± 6.9	-8.4 ± 1.7	-2 ± 0.6	-0.7 ± 0.1	-80 ± 8.5
Fall	7	104.6 ± 4	-18.6 ± 1.8	-0.4 ± 0.2	-1.1 ± 0.1	-137.3 ± 11.2
	15	123.7 ± 8.2	-17.4 ± 2.1	-1.3 ± 0.5	-1.1 ± 0.1	-135.9 ± 11.7
	25	74.4 ± 7.3	-8.4 ± 1.4	-1.6 ± 0.6	-0.6 ± 0.1	-72.3 ± 7.7
	75	98.5 ± 4.8	-13.9 ± 2.1	-0.8 ± 0.5	-1 ± 0.1	-116.3 ± 10.1

Modelled exchange fluxes followed general mineralization patterns outlined above, with highest oxygen (in)fluxes closest to the turbine, ranging from 104.6 ± 4 mmol O_2 m^{-2} d^{-1} in fall to 115.1 ± 3.2 mmol O_2 m^{-2} d^{-1} in summer (Table 8). In line with this, ammonia (NH_3) (ef)fluxes resulting from mineralization were also highest nearest to the turbine (-23.6 ± 1.6, -17.2 ± 2.2, and -18.6 ± 1.8 mmol N m^{-2} d^{-1} in spring, summer and fall respectively), with lower values further away. Nitrate (NO_3^-) fluxes were more variable, with influxes into the sediment in spring (7 and 25 m, 1.2 ± 0.2 and 0.8 ± 0.2 mmol N m^{-2} d^{-1}) and summer (7 m, 0 ± 0.5 mmol N m^{-2} d^{-1}), and consistent effluxes in the other instances (range: -0.2 ± 0.3 mmol N m^{-2} d^{-1} in spring – 15 m to -2 ± 0.6 mmol N m^{-2} d^{-1} in summer – 25 m).

3.6 Graphical exploration of relationships with environment

Model outputs exhibited variable relationships with environmental predictors, with several consistent directional patterns emerging despite substantial variability (Figure S. 14 – S. 18).

https://doi.org/10.5194/egusphere-2026-3576
Preprint. Discussion started: 31 July 2026

A clear trend was observed with distance from the SPL, where total, oxic, and anoxic mineralization generally decreased from 7 to 25 m, to similar values at 75 m, and this pattern was consistent across seasons (Figure S. 14 A, B, D).

The percentage of oxic mineralization was generally higher towards lower TOC content values (Figure S. 15 E), whereas the percentage of anoxic mineralization showed the inverse trend, where percentages tended to increase for higher TOC values (Figure S. 15 G).

The percentage of oxic and anoxic mineralization, and denitrification showed trends related to grain size of surface sediments (Figure S. 16). The percentage of oxic mineralization tended to increase with increasing grain size (Figure S. 16, E), whereas the percentage of anoxic mineralization, and denitrification showed the reverse trend (Figure S. 16, G, F).

Organic matter indicators (chlorophyll *a* and pheophorbide concentrations) showed indications of increasing mineralization rates at higher concentrations (Figure S. 17, Figure S. 18 A, total; C, denitrification; D, anoxic), as well as decreasing oxic mineralization €, increasing anoxic mineralization and dentrification (F, G). However, these relationships were variable and associated with wide confidence intervals, particularly at the upper range of observed values which contained the spring values.

4 Discussion

Traditionally, mineralization processes in marine sediments are derived from measurements in sediment cores during incubation experiments, which require cores of sufficient diameter to provide reasonable estimates of biogeochemical transformation rates. This is especially the case in permeable sediments, where experiments need to include mechanisms to mimic the advective flows that occur in natural settings (e.g. Braeckman et al., 2014; Huettel & Gust, 1992; Toussaint et al., 2021). In the immediate vicinity of offshore wind turbines, where strong environmental gradients occur (Lefaible et al., 2025), this was not possible since scientific divers could not recover coarse permeable sands with cores of sufficient diameter (Ø 10 cm and upward). For safety reasons, research vessels with equipment capable of collecting these large samples are not allowed to operate this close to wind turbines in the study area. Hence, a data-driven modelling approach was needed to characterize gradients in diagenetic properties near offshore wind turbines in combination with the data obtained from the smaller core samples.

The permeable nature of these sediments required the use of a model accounting for advective flows. Initial attempts with a model designed for cohesive sediments (an iteration on the widely applied OMEXDIA, Soetaert et al. (1996)), failed in reconciling the low—to very low measured TOC values (Table 5, Figure S. 1), with the presence of elevated nitrate and ammonia values in porewaters (Figure 3). Also, the higher range of C-deposition fluxes seen within the OWF area (Table 4) directly results in too high TOC concentrations when set in the context of cohesive sediments. Even at the lowest estimated deposition rates in the research area, modelled TOC concentrations remained too high and exceeded observed values by an order of magnitude. Porewater nutrient concentrations were similarly overestimated. In contrast, the PermeableDia model, which includes advective flows driven by pressure gradients, provides a more efficient processing of the high organic matter loads by the continuous provision of oxidants, and export of inorganic nutrients. This results in lower residual TOC in the

https://doi.org/10.5194/egusphere-2026-3576
Preprint. Discussion started: 31 July 2026

sediment and elevated porewater nutrient concentrations due to enhanced mineralization, much more in line with the observed conditions.

Below we first discuss the performance and current limitations of the model itself, and afterwards the model results in the context of the offshore wind farm setting.

4.1 Model limitations and performance

Even though PermeableDia is a 2D model, the lack of information about the distribution of biogeochemical species along the sand ripples forced a simplification step in the fitting procedure. To find suitable parameter values we fitted horizontally averaged 2D model outputs to 1D nutrient profiles. This reduces the impact of the complex bedforms on local sediment biogeochemistry and simultaneously assumes that the measured porewater profiles represent some average state of biogeochemical processes across the bedform topography. At least, the measured profiles are themselves averages of three replicates, and the standard deviation of these measurements is used to weigh the model cost during the evaluation; data points with a large standard deviation exert a weaker constraint in the parameter calibration procedure relative to data points with a small standard deviation. Ideally, 2D data could be gathered for biogeochemical species, for example using planar optodes (Glud et al., 1996; Li et al., 2019) and gel probing applications (Santner et al., 2015). However, this would spectacularly increase the complexity of the fieldwork involved in a marine environment with strong hydrodynamics as within the studied OWF.

The model shows a strong sensitivity to bedform topography, which in this instance alters the balance of different mineralization processes for a given deposition flux (Figure S. 2 D, E). In longer, less high sand ripples the pressure gradient is smaller, and exerted on a larger surface resulting in lower advective transport rates (Figure 5 A). Shorter, higher sand ripples on the other hand, allow for higher flowthrough velocities as a larger pressure gradient is exerted on a smaller surface (Figure 5 B). From our results we noted that the ripple length effects dominate the resulting occurrence of different mineralization processes, as the modelled percentage of anoxic mineralization increases with increasing ripple height, similar to ripple length, whereas the sensitivity analysis showed an opposite effect (Figure S. 2 D, E). In this study bedform topography was derived from sediment grain size, which was measured in the different seasons and locations, but these remain empirical relations and not direct observations. In future endeavors, direct observations of bedform topography (e.g. Cook et al., 2007; Kessler et al., 2012) can provide model inputs to finetune the porewater flow fields.

The largest discrepancies between measurements and model results were for the TOC profiles, as measured profiles tended to have their highest values in deeper layers especially in spring (e.g. Figure S. 3; Figure S. 5; Figure S. 9), or remained relatively straight throughout (e.g. Figure S. 4; Figure S. 6). These types of profiles have been observed previously in permeable sediments (Rusch et al., 2000), and were linked to increased percentages of fines in deeper layers, in turn linked to organic carbon content. We do see increasing percentages of fine sediments (d 0.1) with depth in some sampling instances, but these were not consistently linked to increasing TOC values (e.g. 15 m spring and summer, Figure S. 1). It is possible that this is caused by the steady-state assumption explicit in the model. The model indeed requires a given TOC profile to produce the

https://doi.org/10.5194/egusphere-2026-3576
Preprint. Discussion started: 31 July 2026

observed nutrient profiles, resulting in elevated modelled TOC values. In reality, mineralized TOC (no longer observable) leaves traces in the form of mineralization products - the observed nutrient profiles.

An additional explanation for this mismatch is that fine, organic matter rich particles can be transported into the sediment matrix by advective flows (Bacon et al., 1994; Huettel & Rusch, 2000). This process delivers substrate for mineralization directly into deeper sediment layers, creating TOC distributions that display subsurface peaks, instead of the model's default top-down exponential decrease that results from reactive transport affected by surficial biodiffusion. In permeableDia, high biodiffusion rates may act as a proxy for this advective input, since it similarly represents transport of organic matter away from the surface. Indeed, during model fitting we noticed that high biodiffusion values (*Db*) consistently led to better fits to the data, even though permeable sediments generally host low bioturbator species richness and biomass compared to muddy sediments (e.g. Braeckman et al., 2014; Toussaint et al., 2021). To stay within realistic bounds compared to literature, we imposed a realistic but relatively high (for permeable sands) upper limit on *Db*. The persistence of high fitted *Db* values suggests that the model requires a mechanism equivalent to strong downward transport, likely caused by entrainment of fines, to approximate the measured TOC and associated nutrient profiles.

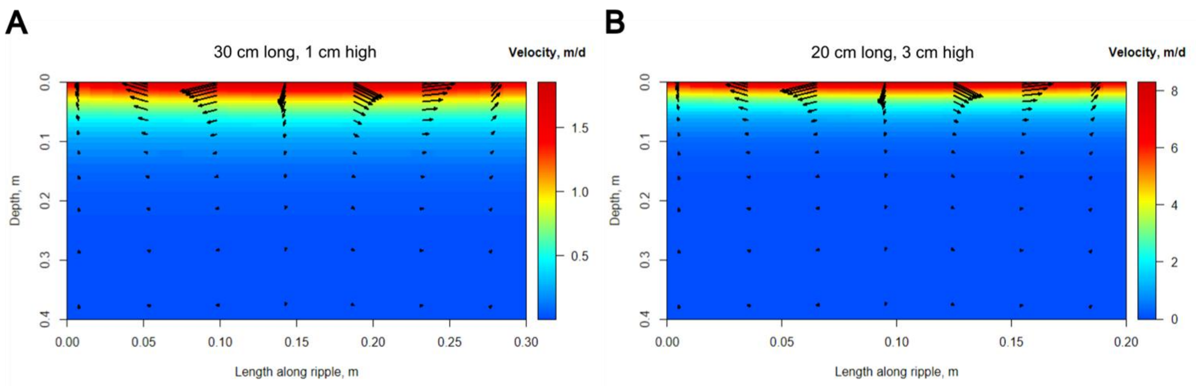

Figure 5: Comparison of flow fields in a ripple with dimensions of 30 cm in length, and 1 cm high (A), and of 20 cm long, and 3 cm high (B).

4.2 Seasonal and distance related patterns

Total mineralization rates evolved throughout the year as expected for the study area (Braeckman et al., 2014; Provoost et al., 2013). In spring organic matter content in the sediment was highest (chlorophyll *a*, TOC), in line with the recent deposition of fresh organic matter, but mineralization process rates were lower compared to later seasons, as they are transitioning from cold temperatures (bottom water temperature 8-9 °C in spring). Water temperatures increased in summer - early fall (18-20 °C), driving higher mineralization rates in these model simulations, while simultaneously depleting the organic matter in the sediment (Table 5, Table 7).

Modelled total mineralization rates displayed trends related to distance to the turbine. Total mineralization was highest closest to the turbine, after which values dropped strongly (Table 7, Figure S. 14). Profiles of ammonia, phosphate and nitrate predominantly align with these observations, as they show a clear link to distance from the turbine (Figure 3). For ammonia this was clearest in spring and summer (at 7 m). Higher ammonia and phosphate values in the sediment imply higher mineralization rates producing these compounds. Lower nitrate values close to the turbine (clearest in spring and autumn) imply less oxygenated conditions, as higher mineralization rates consume oxygen first. Why this pattern in nitrate concentrations is not observed in summer is not clear.

High mineralization values naturally corresponded to highest carbon deposition fluxes, fueling mineralization (Table 6), with deposition values of 178 ± 3.9, 148.8 ± 4, and 138.7 ± 8.3 mmol C m^{-2} d^{-1} in spring, summer, and fall respectively. These values exceed averaged annual mineralization rates previously estimated for the Southern North Sea – BPNS region (Table 4) by a factor of 2 – 10. However, these values were still below those of sediment trap observations which estimated potential deposition within the OWF at 341.7 – 1108.3 mmol C m^{-2} d^{-1} (4.1 – 13.3 g OC m^{-2} d^{-1}) (Cepeda Gamela et al., in prep.). In addition to the sediment trap observations, several *in situ* estimates of oxygen consumption in permeable sediments by means of eddy covariance are of similar magnitude as the rates we modelled (Berg & Huettel, 2023; Chipman et al., 2016; Table 9). With eddy covariance, oxygen consumption (and production) rates are measured *in situ*, over a larger sediment surface, thus integrating the effect of advective flows on mineralization pathways over bedform features, similar to our model (Berg, 2003; Berg et al., 2022). Eddy covariance rates for the North Sea specifically are lower than our estimates, but they stem from much greater water depths as well, where less organic deposition and lower current speeds are expected. Oxygen flux measurements obtained by other means, e.g. stirred cores and incubation chambers, or flow-through experiments vary strongly, but bracket our results (Table 9).

In summary, our modeled rates fall within the mid-to-upper range of reported O_2 consumption rates, consistent with the elevated transformation rates typically captured by eddy covariance measurements and supporting the view of permeable sands as biogeochemical hotspots (Boudreau et al., 2001).

Table 9: Literature summary of sediment oxygen uptake rates in permeable sediments in various settings.

Maximal O_2 consumption rate (mmol O_2 m^{-2} d^{-1})	Water depth (m)	Current velocity (m s^{-1})	Study	Comments
Up to 100	3.6	0.2	Berg & Huettel, (2023)	Eddy covariance in megaripple field
10 – 283	2	< 0.1	Chipman et al. (2016)	Eddy covariance on organic poor sands
30	74	0.11	McGinnis et al. (2014)	Eddy covariance in North Sea
10	120	n.d.	Dale et al. (2021)	Eddy covariance in North Sea
7 ± 6	12 – 27	0.5	Braeckman et al. (2014)	Core incubations with stirring disc in BPNS
14 – 29	20 – 23	0.5	Toussaint et al. (2021)	Core incubations with stirring disc in BPNS
37 ± 29	16	0.2 – 0.35	Janssen (2004)	In situ stirred incubation chambers
> 100	0.5	0.8 (max.)	(Cook et al., 2007)	In situ stirred incubation chambers
49 - 175	1 - 2	0.1	de Beer et al. (2005)	Lower range from stirred incubation chambers, higher rates from core perfusions
39 - 124	**25**	**0.6**	**This study**	**Data driven diagenetic model**

The pattern of decreasing mineralization rates away from the turbine implies that there is a source of organic matter closer to the turbine, which is present throughout the measurement period (April – October). Indeed, highest TOC and chlorophyll a

https://doi.org/10.5194/egusphere-2026-3576
Preprint. Discussion started: 31 July 2026

values occur in spring and summer at 7 m, especially in subsurface values, again indicating the potential role of advective input of organic material (Table 5, Table S. 5). In autumn, these distance-based differences are not present, as most organic materials have likely already been mineralised.

Organic enrichment around offshore wind turbines is likely driven by a combination of biodeposition and hydrodynamic processes. Biodeposition originates from suspension feeders such as *Mytilus edulis* (the blue mussel) that colonize turbine foundations, which produce fecal and pseudo-fecal pellets that sink rapidly and can accumulate in the surrounding sediment (Callier et al., 2006; Liutkus et al., 2012). Given the high filtration capacity of these communities (19000 m^3 of water per turbine per day, Voet et al. (2022), substantial biodeposition is expected. These pellets are often rich in algal pigments, particularly during periods of high primary production, and are known to elevate pigment concentrations in sediments near mussel aggregations such as aquaculture installations (Callier et al., 2006; Cole et al., 2023; Giles et al., 2006; Navarro & Thompson, 1997). In addition, the fouling fauna can also be dislodged (Dannheim et al., 2025) and end up in patches in the sediment, contributing to a temporary organic enrichment.

In addition to biodeposition, turbine-induced hydrodynamic effects may influence the transport and deposition of suspended material. Turbulence generated in the wake of turbine structures alters vertical mixing and can affect both vertical salinity and temperature gradients in the water column (Hendriks et al., 2025), and settling behavior of particles (Legrand et al., 2018). In addition, the drag induced by offshore infrastructure can locally affect tidal currents and bottom stress (Denis et al., 2025). For fine, organic-rich particles, this may have contrasting effects that depend on the exact environmental setting. Increased turbulence can prolong suspension and promote downstream transport before deposition (van Maren et al., 2020), but may also reduce net residual current velocities, enhancing local settling behind the turbine (Legrand et al., 2018). Consequently, it is not possible to determine whether biodeposition or hydrodynamic processes contribute to elevated mineralization rates closest to the turbine, with both mechanisms likely contributing.

Regardless of the source, elevated concentrations of organic matter in the sediment closest to the SPL correspond to highest modelled mineralization rates. This adds to existing evidence that turbine-associated processes influence not only pelagic communities, but also enhance the flux of organic matter to the sediment, altering benthic biogeochemistry both within and beyond OWF boundaries (Coates et al., 2014; De Borger et al., 2021; Ivanov et al., 2021; Slavik et al., 2019). Grain size, a known driver of biogeochemical process rates (e.g. Ahmerkamp et al., 2020; Toussaint et al., 2021), was not correlated to distance from the turbine (in contrast to the findings of Lefaible et al. (2025), which concentrated on the fall data), suggesting that this specific distance effect was primarily driven by organic matter dynamics rather than sediment structure.

Nevertheless, graphic exploration of the relationships of our model outputs with the environment indicated that grain size exerted a clear influence on the relative contribution of mineralization pathways (Figure S. 16). The percentage of oxic mineralization tended to increase with increasing grain size, whereas the percentages of anoxic mineralization and denitrification decrease. This is a result of both the physical effect of increasing grain size; a greater permeability which allows for efficient provision of oxygen to mineralization processes (e.g. Ahmerkamp et al., 2020; de Beer et al., 2005; Toussaint et

https://doi.org/10.5194/egusphere-2026-3576
Preprint. Discussion started: 31 July 2026

al., 2021), and the association of finer sediment particles with higher organic matter loads (which increase the demand for other oxidants) (Mayer, 1994).

Overall, these findings indicate that enhanced organic matter deposition near turbine foundations is efficiently processed by the elevated mineralization rates sustained in permeable sediments under advective flow conditions. This strengthens the view of permeable sediments as highly dynamic processing systems, where increased inputs are rapidly recycled rather than accumulated. Given these high turnover rates, the currently estimated enrichment of ~7-11 % of organic carbon over baseline conditions in the seafloor of this offshore wind farm (Braeckman et al., in prep.; De Borger et al., 2021, 2025) is likely transient. Once the source of enhanced deposition disappears or diminishes, such as under decommissioning scenarios, this excess organic carbon pool is expected to be depleted in several years, to decadal timescales at most.

5 Conclusions

By combining a model with data collected in the field, we demonstrate that mineralization in permeable sediments within the offshore wind farm is particularly intense in the near-turbine zone, where elevated TOC and chlorophyll *a* loads indicate enhanced organic matter deposition. This enrichment is consistent with biodeposition from turbine-associated suspension feeders and (-or) hydrodynamic wake effects that promote particle settling. Beyond this local footprint, mineralization followed expected seasonal patterns of organic matter supply and temperature.

Our modelling results confirm the broader view of permeable sediments as biogeochemical hotspots, to which turbine-induced enrichment adds an additional layer of intensity and spatial variability. Although our modelling approach necessarily simplifies bedform complexity (as we lacked spatially resolved 2D porewater data, for example), the high mineralization rates reproduced by PermeableDia are consistent with independent oxygen flux measurements in permeable sediments from a variety of measurement techniques, and with elevated deposition inferred from sediment trap deployments.

By applying PermeableDia, we also present an open-source, user-friendly framework for quantifying benthic mineralization in permeable sediments under advective flow conditions. This approach can be extended to future studies, bridging gaps where direct measurements are logistically challenging.

Code and data availability

Field-data used in this work are available at https://doi.org/10.24417/bmdc.be:dataset:3147. Code will be provided in a github repository and an R package on the CRAN platform upon eventual publication of the manuscript.

Competing interests

UB is a co-editor of the journal of Biogeosciences. There are no other conflicts of interest to report.

Acknowledgements

Fieldwork would not have been possible without the support and efficient operations of the officers and crew aboard the RV *Belgica*, owned by the Belgian Science Policy Office and coordinated by RBINS–OD Nature, as well as the RV *Simon Stevin*, owned by the Flemish Government and coordinated by VLIZ. The sampling was performed by the Belgian Occupational Scientific Diving team, coordinated by Dr. Alain Norro (RBINS) and Sven Van Haelst (VLIZ), which is part of the contribution of the Institute of Natural Sciences to EMBRC Belgium. We thank the operators of C-Power for their cooperation during sampling, in accordance with the monitoring requirements of their environmental permit. We are also grateful to Bruno Vlaeminck for pigment analyses and to Bart Beuselinck for granulometry, nutrient, and TOC measurements.

Financial support

This research and sample processing were carried out using infrastructure funded by EMBRC Belgium (FWO international research infrastructure I001621N). Additional support was provided by the Belgian Science Policy Office (BELSPO), the OUTFLOW project, and the WinMon.BE monitoring program. This study also contributes to the BELSPO FED-tWIN METRIC project: *Marine Ecosystem Responses in a Multiple Pressures Context*.
EDB was supported by grants of the Belgian Science Policy Office (BELSPO, grants RV/21/CANOE, B2 212/P1 TANGO, and B2 212/P1 OUTFLOW).
AC is funded by the Belspo FedTwin Program, project Prf-2019-008 RECAP.

Author contributions

EDB: Methodology, formal analysis, writing-original draft and review and editing. KS: Software development, writing-review and editing. ECG: Data collection, writing-review and editing. AC: Methodology, writing-review and editing. JV: Conceptualization, funding acquisition, writing-review and editing. UB: Conceptualization, funding acquisition, data collection, writing-review and editing.

References

Ahmerkamp, S., Marchant, H., Peng, C., Probandt, D., Littmann, S., Kuypers, M., & Holtappels, M. (2020). The effect of sediment grain properties and porewater flow on microbial abundance and respiration in permeable sediments. *Scientific Reports*, *10*. https://doi.org/10.1038/s41598-020-60557-7

https://doi.org/10.5194/egusphere-2026-3576
Preprint. Discussion started: 31 July 2026

Ait Ballagh, F. E., Rabouille, C., Andrieux-Loyer, F., Soetaert, K., Elkalay, K., & Khalil, K. (2020). Spatio-temporal dynamics of sedimentary phosphorus along two temperate eutrophic estuaries: A data-modelling approach. *Continental Shelf Research*, *193*, 104037. https://doi.org/10.1016/j.csr.2019.104037

Arndt, S., Jørgensen, B. B., LaRowe, D. E., Middelburg, J. J., Pancost, R. D., & Regnier, P. (2013). Quantifying the degradation of organic matter in marine sediments: A review and synthesis. *Earth-Science Reviews*, *123*, 53–86. https://doi.org/10.1016/j.earscirev.2013.02.008

Bacon, M. P., Belastock, R. A., & Bothner, M. H. (1994). 210Pb balance and implications for particle transport on the continental shelf, U.S. Middle Atlantic Bight. *Deep Sea Research Part II: Topical Studies in Oceanography*, *41*(2), 511–535. https://doi.org/10.1016/0967-0645(94)90033-7

Baretta, J. W., Ebenhöh, W., & Ruardij, P. (1995). The European regional seas ecosystem model, a complex marine ecosystem model. *Netherlands Journal of Sea Research*, *33*(3), 233–246. https://doi.org/10.1016/0077-7579(95)90047-0

Berg, P. (2003). Dynamic Modeling of Early Diagenesis and Nutrient Cycling. A Case Study in an Artic Marine Sediment. *American Journal of Science - AMER J SCI*, *303*, 905–955. https://doi.org/10.2475/ajs.303.10.905

Berg, P., & Huettel, M. (2023). Coastal marine megaripple fields are metabolic hotspots with highly dynamic oxygen exchange. *Limnology and Oceanography Letters*, *8*. https://doi.org/10.1002/lol2.10345

Berg, P., Huettel, M., Glud, R. N., Reimers, C. E., & Attard, K. M. (2022). Aquatic Eddy Covariance: The Method and Its Contributions to Defining Oxygen and Carbon Fluxes in Marine Environments. *Annual Review of Marine Science*, *14*, 431–455. https://doi.org/10.1146/annurev-marine-042121-012329

Boudreau, B. (1997). Diagenetic Models and Their Implementation. In *Springer*. https://doi.org/10.1007/978-3-642-60421-8

Boudreau, B. P., Huettel, M., Forster, S., Jahnke, R. A., McLachlan, A., Middelburg, J. J., Nielsen, P., Sansone, F., Taghon, G., Van Raaphorst, W., Webster, I., Weslawski, J. M., Wiberg, P., & Sundby, B. (2001). Permeable marine sediments: Overturning an old paradigm. *Eos, Transactions American Geophysical Union*, *82*(11), 133–136. https://doi.org/10.1029/EO082i011p00133-01

Braeckman, U., Foshtomi, M. Y., Van Gansbeke, D., Meysman, F., Soetaert, K., Vincx, M., & Vanaverbeke, J. (2014). Variable Importance of Macrofaunal Functional Biodiversity for Biogeochemical Cycling in Temperate Coastal Sediments. *Ecosystems*, *17*(4), 720–737. https://doi.org/10.1007/s10021-014-9755-7

Braeckman, U., Van Den Eynde, D., Gamela, E. C., De Borger, E., Capet, A., & Vanaverbeke, J. (in prep.). *Linking hydrodynamics and biodeposition: Organic matter accumulation around offshore wind turbine foundations* [Unpublished manuscript].

Brand, A., Lewandowski, J., Hamann, E., & Nützmann, G. (2013). Advection around ventilated U-shaped burrows: A model study. *Water Resources Research*, *49*(5), 2907–2917. https://doi.org/10.1002/wrcr.20266

Callier, M. D., Weise, A. M., McKindsey, C. W., & Desrosiers, G. (2006). Sedimentation rates in a suspended mussel farm (Great-Entry Lagoon, Canada): Biodeposit production and dispersion. *Marine Ecology Progress Series*, *322*, 129–141. https://doi.org/10.3354/meps322129

https://doi.org/10.5194/egusphere-2026-3576
Preprint. Discussion started: 31 July 2026

Capet, A., Meysman, F. J. R., Akoumianaki, I., Soetaert, K., & Grégoire, M. (2016). Integrating sediment biogeochemistry into 3D oceanic models: A study of benthic-pelagic coupling in the Black Sea. *Ocean Modelling*, *101*, 83–100. https://doi.org/10.1016/j.ocemod.2016.03.006

Cardenas, M. B., Cook, P. L. M., Jiang, H., & Traykovski, P. (2008). Constraining denitrification in permeable wave-influenced marine sediment using linked hydrodynamic and biogeochemical modeling. *Earth and Planetary Science Letters*, *275*(1), 127–137. https://doi.org/10.1016/j.epsl.2008.08.016

Chipman, L., Berg, P., & Huettel, M. (2016). Benthic Oxygen Fluxes Measured by Eddy Covariance in Permeable Gulf of Mexico Shallow-Water Sands. *Aquatic Geochemistry*, *22*(5–6), 529–554. https://doi.org/10.1007/s10498-016-9305-3

Chowdhury, F., Gong, J., Rau, G. C., & Timms, W. A. (2022). Multifactor analysis of specific storage estimates and implications for transient groundwater modelling. *Hydrogeology Journal*, *30*, 2183. https://doi.org/10.1007/s10040-022-02535-z

Chua, E. J., Huettel, M., Fennel, K., & Fulweiler, R. W. (2022). A case for addressing the unresolved role of permeable shelf sediments in ocean denitrification. *Limnology and Oceanography Letters*, *7*(1), 11–25. https://doi.org/10.1002/lol2.10218

Coates, D. A., Deschutter, Y., Vincx, M., & Vanaverbeke, J. (2014). Enrichment and shifts in macrobenthic assemblages in an offshore wind farm area in the Belgian part of the North Sea. *Marine Environmental Research*, *95*, 1–12. https://doi.org/10.1016/j.marenvres.2013.12.008

Cole, M., Artioli, Y., Coppock, R., Galli, G., Saad, R., Torres, R., Vance, T., Yunnie, A., & Lindeque, P. K. (2023). Mussel power: Scoping a nature-based solution to microplastic debris. *Journal of Hazardous Materials*, *453*, 131392. https://doi.org/10.1016/j.jhazmat.2023.131392

Cook, P. L. M., Wenzhöfer, F., Glud, R. N., Janssen, F., & Huettel, M. (2007). Benthic solute exchange and carbon mineralization in two shallow subtidal sandy sediments: Effect of advective pore-water exchange. *Limnology and Oceanography*, *52*(5), 1943–1963. https://doi.org/10.4319/lo.2007.52.5.1943

Cook, P. L. M., Wenzhöfer, F., Rysgaard, S., Galaktionov, O. S., Meysman, F. J. R., Eyre, B. D., Cornwell, J., Huettel, M., & Glud, R. N. (2006). Quantification of denitrification in permeable sediments: Insights from a two-dimensional simulation analysis and experimental data. *Limnology and Oceanography: Methods*, *4*(9), 294–307. https://doi.org/10.4319/lom.2006.4.294

Dale, A. W., Sommer, S., Lichtschlag, A., Koopmans, D., Haeckel, M., Kossel, E., Deusner, C., Linke, P., Scholten, J., Wallmann, K., van Erk, M. R., Gros, J., Scholz, F., & Schmidt, M. (2021). Defining a biogeochemical baseline for sediments at Carbon Capture and Storage (CCS) sites: An example from the North Sea (Goldeneye). *International Journal of Greenhouse Gas Control*, *106*, 103265. https://doi.org/10.1016/j.ijggc.2021.103265

Dannheim, J., Beermann, J., Coolen, J. W. P., Vanaverbeke, J., Degraer, S., Birchenough, S. N. R., Garcia, C., Lacroix, G., Fiorentino, D., Lindeboom, H., Krone, R., Pehlke, H., Braeckman, U., & Brey, T. (2025). Offshore wind turbines constitute benthic secondary production hotspots on and around constructions. *Journal of Environmental Management*, *393*, 126922. https://doi.org/10.1016/j.jenvman.2025.126922

https://doi.org/10.5194/egusphere-2026-3576
Preprint. Discussion started: 31 July 2026

de Beer, D., Wenzhöfer, F., Ferdelman, T. G., Boehme, S. E., Huettel, M., van Beusekom, J. E. E., Böttcher, M. E., Musat, N., & Dubilier, N. (2005). Transport and mineralization rates in North Sea sandy intertidal sediments, Sylt-Rømø Basin, Wadden Sea. *Limnology and Oceanography*, *50*(1), 113–127. https://doi.org/10.4319/lo.2005.50.1.0113

De Borger, E., Ivanov, E., Capet, A., Braeckman, U., Vanaverbeke, J., Grégoire, M., & Soetaert, K. (2021). Offshore Windfarm Footprint of Sediment Organic Matter Mineralization Processes. *Frontiers in Marine Science*, *8*. https://doi.org/10.3389/fmars.2021.632243

De Borger, E., van Oevelen, D., Mavraki, N., De Backer, A., Braeckman, U., Soetaert, K., & Vanaverbeke, J. (2025). Offshore wind farms modify coastal food web dynamics by enhancing suspension feeder pathways. *Communications Earth & Environment*, *6*(1), 1–16. https://doi.org/10.1038/s43247-025-02253-w

De Mesel, I., Kerckhof, F., Norro, A., Rumes, B., & Degraer, S. (2015). Succession and seasonal dynamics of the epifauna community on offshore wind farm foundations and their role as stepping stones for non-indigenous species. *Hydrobiologia*, *756*(1), 37–50. https://doi.org/10.1007/s10750-014-2157-1

Degraer, S., Carey, D., Coolen, J., Hutchison, Z., Kerckhof, F., Rumes, B., & Vanaverbeke, J. (2020). Offshore Wind Farm Artificial Reefs Affect Ecosystem Structure and Functioning: A Synthesis. *Oceanography*, *33*(4), 48–57. https://doi.org/10.5670/oceanog.2020.405

Denis, P., Capet, A., Vanaverbeke, J., Kerkhove, T. R. H., Lacroix, G., & Legrand, S. (2025). Hydrodynamic alterations induced by floating solar structures co-located with an offshore wind farm. *Frontiers in Marine Science*, *12*. https://doi.org/10.3389/fmars.2025.1674859

Dickens, G. R., Koelling, M., Smith, D. C., Schnieders, L., & the IODP Expedition 302 Scientists. (2007). Rhizon Sampling of Pore Waters on Scientific Drilling Expeditions: An Example from the IODP Expedition 302, Arctic Coring Expedition (ACEX). *Scientific Drilling*, *4*, 22–25. https://doi.org/10.2204/iodp.sd.4.08.2007

Dunne, J. P., Sarmiento, J. L., & Gnanadesikan, A. (2007). A synthesis of global particle export from the surface ocean and cycling through the ocean interior and on the seafloor. *Global Biogeochemical Cycles*, *21*(4). https://doi.org/10.1029/2006GB002907

Emery, K. O. (1968). Relict Sediments on Continental Shelves of World1. *AAPG Bulletin*, *52*(3), 445–464. https://doi.org/10.1306/5D25C2E7-16C1s-11D7-8645000102C1865D

Frossard, J., & Renaud, O. (2021). Permutation Tests for Regression, ANOVA, and Comparison of Signals: The **permuco** Package. *Journal of Statistical Software*, *99*(15). https://doi.org/10.18637/jss.v099.i15

Giles, H., Pilditch, C. A., & Bell, D. G. (2006). Sedimentation from mussel (*Perna canaliculus*) culture in the Firth of Thames, New Zealand: Impacts on sediment oxygen and nutrient fluxes. *Aquaculture*, *261*(1), 125–140. https://doi.org/10.1016/j.aquaculture.2006.06.048

Glud, R. N., Ramsing, N. B., Gundersen, J. K., & Klimant, I. (1996). Planar optrodes: A new tool for fine scale measurements of two- dimensional O2 distribution in benthic communities. *Marine Ecology Progress Series*, *140*(1–3), 217–226. https://doi.org/10.3354/meps140217

Gomez, J. D., Wilson, J. L., & Cardenas, M. B. (2012). Residence time distributions in sinuosity-driven hyporheic zones and their biogeochemical effects. *Water Resources Research*, *48*(9). https://doi.org/10.1029/2012WR012180

Gridded Bathymetry Data | GEBCO. (2024). https://www.gebco.net/data-products/gridded-bathymetry-data

Hendriks, E., Langedock, K., van Duren, L. A., Vanaverbeke, J., Boone, W., & Soetaert, K. (2025). The impact of offshore wind turbine foundations on local hydrodynamics and stratification in the Southern North Sea. *Frontiers in Marine Science*, *12*. https://doi.org/10.3389/fmars.2025.1619577

Huettel, M., Berg, P., & Kostka, J. E. (2014). Benthic Exchange and Biogeochemical Cycling in Permeable Sediments. *Annual Review of Marine Science*, *6*(Volume 6, 2014), 23–51. https://doi.org/10.1146/annurev-marine-051413-012706

Huettel, M., & Gust, G. (1992). Solute release mechanisms from confined sediment cores in stirred benthic chambers and flume flows. *Marine Ecology Progress Series*, *82*, 187–197. https://doi.org/10.3354/meps082187

Huettel, M., & Rusch, A. (2000). Transport and degradation of phytoplankton in permeable sediment. *Limnology and Oceanography*, *45*(3), 534–549. https://doi.org/10.4319/lo.2000.45.3.0534

Ivanov, E., Capet, A., Borger, E. D., Degraer, S., Delhez, E. J. M., Soetaert, K., Vanaverbeke, J., & Grégoire, M. (2021). Offshore Wind Farm Footprint on Organic and Mineral Particle Flux to the Bottom. *Frontiers in Marine Science*, *8*. https://doi.org/10.3389/fmars.2021.631799

Janssen, F. (2004). *Pore-water advection and organic matter mineralization in North Sea shelf sands* [Max-Planck-Institut]. https://pure.mpg.de/rest/items/item_2485918/component/file_3253960/content

Jodo, M., Kawamoto, K., Tochimoto, M., & Coverly, S. C. (1992). Determination of nutrients in seawater by segmented–flow analysis with higher analysis rate and reduced interference on ammonia. *Journal of Analytical Methods in Chemistry*, *14*(5), 964507. https://doi.org/10.1155/S1463924692000300

Joiris, C., Billen, G., Lancelot, C., Daro, M. H., Mommaerts, J. P., Bertels, A., Bossicart, M., Nijs, J., & Hecq, J. H. (1982). A budget of carbon cycling in the Belgian coastal zone: Relative roles of zooplankton, bacterioplankton and benthos in the utilization of primary production. *Netherlands Journal of Sea Research*, *16*, 260–275. https://doi.org/10.1016/0077-7579(82)90035-7

Kerckhof, F., Rumes, B., Jacques, T., Degraer, S., & Norro, A. (2010). Early development of the subtidal marine biofouling on a concrete offshore windmill foundation on the Thornton Bank (southern North Sea): First monitoring results. *Underwater Technology*, *29*(3), 137–149. https://doi.org/10.3723/ut.29.137

Kessler, A. J., Cardenas, M. B., & Cook, P. L. M. (2015). The negligible effect of bed form migration on denitrification in hyporheic zones of permeable sediments. *Journal of Geophysical Research: Biogeosciences*, *120*(3), 538–548. https://doi.org/10.1002/2014JG002852

Kessler, A. J., Glud, R. N., Cardenas, M. B., Larsen, M., Bourke, M. F., & Cook, P. L. M. (2012). Quantifying denitrification in rippled permeable sands through combined flume experiments and modeling. *Limnology and Oceanography*, *57*(4), 1217–1232. https://doi.org/10.4319/lo.2012.57.4.1217

Lancelot, C., Spitz, Y., Gypens, N., Ruddick, K., Becquevort, S., Rousseau, V., Lacroix, G., & Billen, G. (2005). Modelling diatom and Phaeocystis blooms and nutrient cycles in the Southern Bight of the North Sea: The MIRO model. *Marine Ecology Progress Series*, *289*, 63–78. https://doi.org/10.3354/meps289063

Lefaible, N., Van Colen, C., Jammar, C., Vanaverbeke, J., Moens, T., Van Haelst, S., Norro, A., Degraer, S., & Braeckman, U. (2025). Laying out the foundations: Assessing the spatial extent and drivers of offshore wind turbine artificial reef effects on soft sediments. *Journal of Sea Research*, *208*, 102631. https://doi.org/10.1016/j.seares.2025.102631

Legrand, S., de la Vallée, P., Fettweis, M., & Van den Eynde, D. (2018). *Actualisation de l'évaluation initiale pour les eaux marines belges* (2.5. Changements Hydrographiques (D7), p. 62). UGMM, Service Public Fédéral Santé publique, Sécurité de la Chaîne alimentaire et Environnement,.

Li, C., Ding, S., Yang, L., Zhu, Q., Chen, M., Tsang, D. C. W., Cai, G., Feng, C., Wang, Y., & Zhang, C. (2019). Planar optode: A two-dimensional imaging technique for studying spatial-temporal dynamics of solutes in sediment and soil. *Earth-Science Reviews*, *197*, 102916. https://doi.org/10.1016/j.earscirev.2019.102916

Liutkus, M., Robinson, S., MacDonald, B., & Reid, G. (2012). Quantifying the Effects of Diet and Mussel Size on the Biophysical Properties of the Blue Mussel, Mytilus spp., Feces Egested Under Simulated Imta Conditions. *Journal of Shellfish Research*, *31*(1), 69–77. https://doi.org/10.2983/035.031.0109

Loeff, M. M. R. van der. (1981). Wave Effects on Sediment Water Exchange in a Submerged Sand Bed. In *Regeneration of nutrients in Dutch coastal sediments* (pp. 100–112). Brill. https://doi.org/10.1163/9789004582910_005

Lohse, L., Epping, E., Helder, W., & Van Raaphorst, W. (1996). Oxygen pore water profiles in continental shelf sediments of the North Sea:turbulent versus molecular diffusion. *Marine Ecology Progress Series*, *145*, 63–75. https://doi.org/10.3354/meps145063

Maar, M., Bolding, K., Petersen, J. K., Hansen, J. L. S., & Timmermann, K. (2009). Local effects of blue mussels around turbine foundations in an ecosystem model of Nysted off-shore wind farm, Denmark. *Journal of Sea Research, Metabolic Organization: 30 Years of DEB Applications and Developments*, *62*(2), 159–174. https://doi.org/10.1016/j.seares.2009.01.008

Mavraki, N., De Mesel, I., Degraer, S., Moens, T., & Vanaverbeke, J. (2020). Resource Niches of Co-occurring Invertebrate Species at an Offshore Wind Turbine Indicate a Substantial Degree of Trophic Plasticity. *Frontiers in Marine Science*, *7*, 379. https://doi.org/10.3389/fmars.2020.00379

Mayer, L. M. (1994). Surface area control of organic carbon accumulation in continental shelf sediments. *Geochimica et Cosmochimica Acta*, *58*(4), 1271–1284. https://doi.org/10.1016/0016-7037(94)90381-6

McGinnis, D. F., Sommer, S., Lorke, A., Glud, R. N., & Linke, P. (2014). Quantifying tidally driven benthic oxygen exchange across permeable sediments: An aquatic eddy correlation study. *Journal of Geophysical Research: Oceans*, *119*(10), 6918–6932. https://doi.org/10.1002/2014JC010303

Meile, C. (2003). Explicit representation of spatial heterogeneity in reactive transport models: Application to bioirrigated sediments. *Journal of Geochemical Exploration*.

https://doi.org/10.5194/egusphere-2026-3576
Preprint. Discussion started: 31 July 2026

https://www.academia.edu/15442540/Explicit_representation_of_spatial_heterogeneity_in_reactive_transport_models_application_to_bioirrigated_sediments

Meysman, F. J. R., Galaktionov, O. S., Cook, P. L. M., Janssen, F., Huettel, M., & Middelburg, J. J. (2007). *Quantifying biologically and physically induced flow and tracer dynamics in permeable sediments*.

Meysman, F. J. R., Galaktionov, O. S., & Middelburg, J. J. (2005). Irrigation patterns in permeable sediments induced by burrow ventilation: A case study of Arenicola marina. *Marine Ecology Progress Series*, *303*, 195–212. https://doi.org/10.3354/meps303195

Middelburg, J. J. (2019). *Marine Carbon Biogeochemistry: A Primer for Earth System Scientists*. Springer International Publishing. https://doi.org/10.1007/978-3-030-10822-9

Navarro, J. M., & Thompson, R. J. (1997). Biodeposition by the horse mussel *Modiolus modiolus* (Dillwyn) during the spring diatom bloom. *Journal of Experimental Marine Biology and Ecology*, *209*(1), 1–13. https://doi.org/10.1016/0022-0981(96)02681-0

Paraska, D. W., Hipsey, M. R., & Salmon, S. U. (2014). Sediment diagenesis models: Review of approaches, challenges and opportunities. *Environmental Modelling & Software*, *61*, 297–325. https://doi.org/10.1016/j.envsoft.2014.05.011

Peire, K., Nonneman, H., & Bosschem, E. (2009). Gravity base foundations for the Thornton Bank offshore wind farm. *Terra et Aqua*, (115).

Posit team. (2022). *RStudio: Integrated Development Environment for R*. Posit Software, PBC. http://www.posit.co/

Precht, E., & Huettel, M. (2004). Rapid wave-driven advective pore water exchange in a permeable coastal sediment. *Journal of Sea Research*, *51*(2), 93–107. https://doi.org/10.1016/j.seares.2003.07.003

Provoost, P., Braeckman, U., Van Gansbeke, D., Moodley, L., Soetaert, K., Middelburg, J. J., & Vanaverbeke, J. (2013). Modelling benthic oxygen consumption and benthic-pelagic coupling at a shallow station in the southern North Sea. *Estuarine, Coastal and Shelf Science*, *120*, 1–11. https://doi.org/10.1016/j.ecss.2013.01.008

R Core Team. (2021). *R: A Language and Environment for Statistical Computing*. R Foundation for Statistical Computing. https://www.R-project.org/

RBINS metadata catalog. (2025). https://metadata.naturalsciences.be/geonetwork/srv/eng/catalog.search#/home

Ren, J., & Packman, A. I. (2004). Modeling of simultaneous exchange of colloids and sorbing contaminants between streams and streambeds. *Environmental Science & Technology*, *38*(10), 2901–2911. https://doi.org/10.1021/es0348521

Ren, J., & Packman, A. I. (2005). Coupled stream-subsurface exchange of colloidal hematite and dissolved zinc, copper, and phosphate. *Environmental Science & Technology*, *39*(17), 6387–6394. https://doi.org/10.1021/es050168q

Rusch, A., Huettel, M., & Forster, S. (2000). Particulate Organic Matter in Permeable Marine Sands—Dynamics in Time and Depth. *Estuarine, Coastal and Shelf Science*, *51*(4), 399–414. https://doi.org/10.1006/ecss.2000.0687

Rutherford, J. C., Boyle, J. D., Elliott, A. H., Hatherell, T. V. J., & Chiu, T. W. (1995). Modeling Benthic Oxygen Uptake by Pumping. *Journal of Environmental Engineering*, *121*(1), 84–95. https://doi.org/10.1061/(ASCE)0733-9372(1995)121:1(84)

https://doi.org/10.5194/egusphere-2026-3576
Preprint. Discussion started: 31 July 2026

Santner, J., Larsen, M., Kreuzeder, A., & Glud, R. N. (2015). Two decades of chemical imaging of solutes in sediments and soils – a review. *Analytica Chimica Acta*, *878*, 9–42. https://doi.org/10.1016/j.aca.2015.02.006

Savant, S. A., Reible, D. D., & Thibodeaux, L. J. (1987). Convective transport within stable river sediments. *Water Resources Research*, *23*(9), 1763–1768. https://doi.org/10.1029/WR023i009p01763

Seeberg-Elverfeldt, J., Schlüter, M., Feseker, T., & Kölling, M. (2005). Rhizon sampling of porewaters near the sediment-water interface of aquatic systems. *Limnology and Oceanography: Methods*, *3*(8), 361–371. https://doi.org/10.4319/lom.2005.3.361

Shotbolt, L. (2010). Pore water sampling from lake and estuary sediments using Rhizon samplers. *Journal of Paleolimnology*, *44*(2), 695–700. https://doi.org/10.1007/s10933-008-9301-8

Shum, K. T. (1992). Wave-induced advective transport below a rippled water-sediment interface. *Journal of Geophysical Research: Oceans*, *97*(C1), 789–808. https://doi.org/10.1029/91JC02101

Shum, K. T., & Sundby, B. (1996). Organic matter processing in continental shelf sediments—The subtidal pump revisited. *Marine Chemistry*. https://www.academia.edu/16369975/Organic_matter_processing_in_continental_shelf_sediments_the_subtidal_pump_revisited

Slavik, K., Lemmen, C., Zhang, W., Kerimoglu, O., Klingbeil, K., & Wirtz, K. W. (2019). The large-scale impact of offshore wind farm structures on pelagic primary productivity in the southern North Sea. *Hydrobiologia*, *845*(1), 35–53. https://doi.org/10.1007/s10750-018-3653-5

Soetaert, K., & Herman, P. M. J. (Eds.). (2009). *A Practical Guide to Ecological Modelling*. Springer Netherlands. https://doi.org/10.1007/978-1-4020-8624-3

Soetaert, K., Herman, P. M. J., & Middelburg, J. J. (1996). A model of early diagenetic processes from the shelf to abyssal depths. *Geochimica et Cosmochimica Acta*, *60*(6), 1019–1040. https://doi.org/10.1016/0016-7037(96)00013-0

Soetaert, K., & Petzoldt, T. (2023). *FME: A Flexible Modelling Environment for Inverse Modelling, Sensitivity, Identifiability and Monte Carlo Analysis* (Version 1.3.6.3) [Computer software]. https://cran.r-project.org/web/packages/FME/index.html

Soulsby, R. (1997). *Dynamics of marine sands: A manual for practical applications* (1. publ). Telford.

Soulsby, R. L., Whitehouse, R. J. S., & Marten, K. V. (2012). Prediction of time-evolving sand ripples in shelf seas. *Continental Shelf Research*, *38*, 47–62. https://doi.org/10.1016/j.csr.2012.02.016

Thibodeaux, L. J., & Boyle, J. D. (1987). Bedform-generated convective transport in bottom sediment. *Nature*, *325*, 341–343. https://doi.org/10.1038/325341a0

Toussaint, E., De Borger, E., Braeckman, U., De Backer, A., Soetaert, K., & Vanaverbeke, J. (2021). Faunal and environmental drivers of carbon and nitrogen cycling along a permeability gradient in shallow North Sea sediments. *Science of The Total Environment*, *767*, 144994. https://doi.org/10.1016/j.scitotenv.2021.144994

Van den Eynde, D., Baeye, M., & Van Lancker, V. (2020). *Effect of wind farms on the siltation of gravel beds* (DGENV/X/DVDE/202006/EN/TR01; p. 53). Royal Belgian Institute for Natural Sciences, Operational Directorate Natural

Environment. https://biblio.naturalsciences.be/library-1/rbins-staff-publications-2020/pdfs/Van%20den%20Eynde%20et%20al%202020%20-%20Study%201.1.pdf

van Maren, D. S., Vroom, J., Fettweis, M., & Vanlede, J. (2020). Formation of the Zeebrugge coastal turbidity maximum: The role of uncertainty in near-bed exchange processes. *Marine Geology*, *425*, 106186. https://doi.org/10.1016/j.margeo.2020.106186

Voet, H. E. E., Van Colen, C., & Vanaverbeke, J. (2022). Climate change effects on the ecophysiology and ecological functioning of an offshore wind farm artificial hard substrate community. *Science of The Total Environment*, *810*, 152194. https://doi.org/10.1016/j.scitotenv.2021.152194

Wakelin, S. L., Holt, J. T., Blackford, J. C., Allen, J. I., Butenschön, M., & Artioli, Y. (2012). Modeling the carbon fluxes of the northwest European continental shelf: Validation and budgets. *Journal of Geophysical Research: Oceans*, *117*(C5). https://doi.org/10.1029/2011JC007402

Webb, J. E., & Theodor, J. L. (1972). Wave-induced circulation in submerged sands. *Journal of the Marine Biological Association of the United Kingdom*, *52*(4), 903–914. https://doi.org/10.1017/S0025315400040649

Wright, S. W., & Mantoura, R. F. C. (1997). Guidelines for collection and pigment analysis of field samples. In S. W. Jeffrey, R. F. C. Mantoura, & S. W. Wright, *Phytoplankton pigments in oceanography: Guidelines to modern methods.* (p. 661). UNESCO publishing.

Zhang, W., Porz, L., Yilmaz, R., Wallmann, K., Spiegel, T., Neumann, A., Holtappels, M., Kasten, S., Kuhlmann, J., Ziebarth, N., Taylor, B., Ho-Hagemann, H. T. M., Bockelmann, F.-D., Daewel, U., Bernhardt, L., & Schrum, C. (2024). Long-term carbon storage in shelf sea sediments reduced by intensive bottom trawling. *Nature Geoscience*, *17*(12), 1268–1276. https://doi.org/10.1038/s41561-024-01581-4

Zheng, L., Cardenas, M. B., Wang, L., & Mohrig, D. (2019). Ripple Effects: Bed Form Morphodynamics Cascading Into Hyporheic Zone Biogeochemistry. *Water Resources Research*, *55*(8), 7320–7342. https://doi.org/10.1029/2018WR023517